Contrib Mineral Petrol (2006) 152:541–569
DOI 10.1007/s00410-006-0125-0

ORIGINAL PAPER

A magmatic-hydrothermal transition in Arkaroola (northern Flinders Ranges, South Australia): from diopside–titanite pegmatites to hematite–quartz growth

Ronald J. Bakker · Marlina A. Elburg

Received: 15 October 2005 / Accepted: 14 June 2006 / Published online: 1 August 2006

Abstract A set of Palaeozoic diopside–titanite veins are present in Mesoproterozoic metagranites and metasediments that constitute the basement (Mt Painter Inlier) of the Adelaide Fold Belt (South Australia). These massive veins (up to 1 m) of pegmatitic nature contain large crystals of diopside, *LREE–Y*-enriched titanite (up to 40 cm in length) and minor amounts of quartz. They can be used to trace the system's development from a high-temperature magmatic stage through to a massive hydrothermal event. The pegmatitic origin of these veins is evident from a complex fluid-melt inclusion assemblage, consisting of a highly saline inhomogeneous fluid and relicts of melt. Immiscibility of melt and heterogeneous highly saline fluids (exceeding 61 eq. mass% NaCl) is preserved in primary inclusions in diopside and secondary inclusions in titanite, indicating relatively shallow conditions of formation (510 ± 20°C and 130 ± 10 MPa). Graphic intergrowth of diopside and albite occurs at the contact with granitic pegmatites. The system evolved into hydrothermal conditions, which can be deduced from a later population of only fluid inclusions (homogeneous and less saline, ≈ 40 eq. mass% NaCl), trapped around 350 ± 20°C and 80 ± 10 MPa. During quartz crystallization, the conditions moved across the halite liquidus resulting in a heterogeneous mixture of brine and halite crystals, which were trapped at 200 ± 20°C and 50 ± 10 MPa. Brecciation and a palaeo-geothermal system overprinted the pegmatitic veins with an epithermal hematite–quartz assemblage and lesser amounts of bladed calcite and fluorite, in an intermittently boiling hydrothermal system of fairly pure H_2O at 100–140°C and 1–5 MPa. Remobilization of *LREE*s and *Y* from titanite and/or the granitic host rock is evidenced by precipitation of apatite, allanite and wakefieldite in an intermediate stage. Occasional incorporation of radioactive elements or minerals, presumably U-rich, in the fluorite is responsible for radiolysis of H_2O to H_2.

Communicated by J. Touret

R. J. Bakker (✉)
Department of Applied Geosciences and Geophysics, Mineralogy and Petrology, University of Leoben, Peter-Tunner-Str. 5, 8700 Leoben, Austria
e-mail: bakker@unileoben.ac.at

M. A. Elburg
Department of Geology and Soil Science, Ghent University, Krijgslaan 281 S8, 9000 Ghent, Belgium
e-mail: marlina.elburg@Ugent.be

Introduction

Intrusive rocks are often studied by performing whole rock analyses that are then used to determine the composition of magmatic liquids. Although this method can give good results, the interpretation of whole rock analyses may be complicated by accumulative processes. This whole rock approach is even less suitable to study the late- and post-magmatic evolution of intrusive events, as residual melts and fluids tend to escape to higher structural levels, or loose their identity by interaction with the already crystallized phases, or host rock. Studies of melt and fluid inclusions (e.g. Frezzotti 1992; Thompson 1995) are better suited to understand the late- and post-magmatic history of intrusive rocks. In general, magmatic crystallization

processes involve a marked evolution of associated fluids. These volatiles interact with both crystallized magma and remaining silicate liquids, and some elements and components can be lost or gained from the intruded host rock (e.g. Thompson 1995). Exsolved silicate- and hydrosaline melts (e.g. Panina 2005), in addition to aqueous fluids, may be trapped at a late magmatic stage, and these may evolve into both heterogeneous and homogeneous fluid mixtures during subsequent cooling and uplift of the system. Commonly, these trapped fluids and melts contain concise information about formation conditions of the magma or about related ore deposits within the host rocks, for example in skarns (Baker et al. 2004) or porphyry deposits (Bodnar 1995).

The Mesoproterozoic basement in the northwestern part of the Adelaide Fold Belt (northern Flinders Ranges, South Australia) contains several types of veins and pegmatitic rocks. The occurrence of up to 1.5-m thick diopside–titanite veins in the region north of Arkaroola (Mt Painter Inlier, Fig. 1), which are tectonically reactivated (including brecciation) and overprinted by massive quartz–hematite mineralization (Elburg et al. 2003) is remarkable. The aim of this research is to interpret the evolution of this late magmatic-hydrothermal system that led to the formation of those mineral assemblages, including detailed petrography, mineral-chemistry and fluid and melt inclusion studies. The information about the palaeo-fluid/melt and the formation conditions of diopside–titanite veins and quartz–hematite veins illustrate the transition from a late magmatic to a hydrothermal system within the Mt Painter Inlier.

Geological setting

Located in the northern Flinders Ranges, South Australia, the region of Arkaroola consists of a Palaeo-Mesoproterozoic basement (the Mt Painter Inlier), of granites, gneisses and metasediments, overlain by Neoproterozoic-Cambrian metasediments (Fig. 1). It forms the northernmost part of the

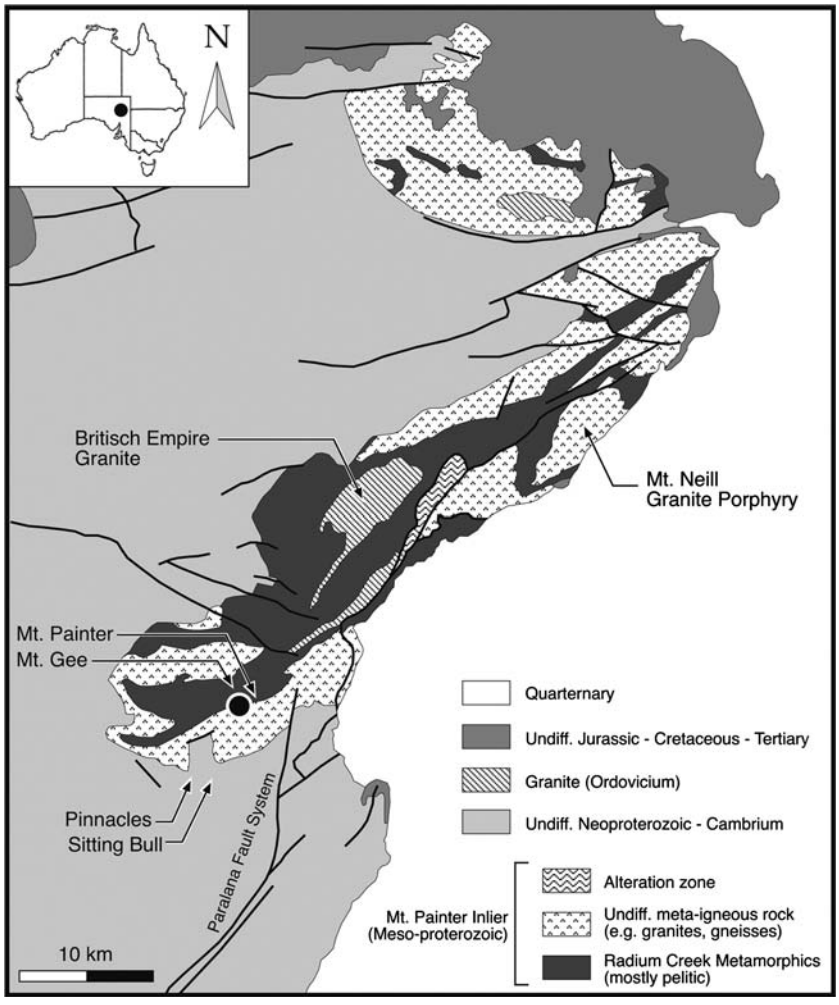

Fig. 1 Geological map of the Mt Painter Inlier (after Coats and Blisset 1971). The *dot* indicates the location of diopside–titanite veins (coordinates 30°14′56.5″S, 139°20′29.2″E) and massive quartz–hematite mineralizations (coordinates 30°13′30.6″S, 139°20′41.7″E)

Adelaide Fold Belt (Coats and Blisset 1971). The metasediments in the basement (Radium Creek metamorphics) are of presumed Palaeoproterozoic age and have been intruded by Mesoproterozoic A-type granites and trondhjemites (Teale 1993), which were locally altered into gneisses and schists in the Palaeozoic (Elburg et al. 2001). The area underwent deformation and high *T*–low *P* metamorphism during the ~ 500 Ma Delamerian Orogeny. This caused growth of metamorphic minerals such as biotite, cordierite and andalusite in the basement and the lowermost units of the Neoproterozoic sequence. High heat production in the basement is related to the presence of uranium-rich granites, and is presumed to have caused a contact metamorphism within the Neoproterozoic cover (e.g. McLaren et al. 2002). The orogeny caused ductile deformation in both basement and cover during prograde metamorphism, which evolved into brittle deformation during subsequent uplift and the development of shear and fault zones. Small volumes of pegmatites and leucogranites intruded the area along fault intersections. This Delamerian event was followed by a localized magmatic-hydrothermal event in the Late Ordovician (~ 440 Ma) (Elburg et al. 2003). During this event, a large I–S type granitic batholith, the British Empire Granite, intruded the Palaeoproterozoic basement. Pegmatite-related uranium mineral assemblages [euxinite series (U, Fe, Y)NbO_4] are the host of primary uranium mineralization in the Mt Painter Inlier for which the age is poorly constrained (462+34/–36 Ma—U–Pb dating monazite, Elburg et al. 2003), but could coincide with that of the diopside–titanite veins (443 ± 3 Ma—U–Pb dating on titanite, Elburg et al. 2003). The waning stages are characterized by skarn formation and epithermal quartz–hematite mineralization (dot in Fig. 1, Mt Gee). The quartz–hematite assemblages are found in large bodies, such as the Mt Gee breccia, but also overprint the diopside–titanite veins. Their age can therefore be constrained to be younger than 440 Ma. The uranium ore is contained in granitic and hematitic breccias (Drexel and Major 1990), and is also crosscut by this quartz–hematite association. It seems likely that a significant part of the uranium, like the REE, in these pegmatitic minerals was derived from the Mesoproterozoic A-type granites that host the mineralization. The quartz–hematite breccia and uranium mineral assemblages have previously drawn attention because of their similarity to the giant Olympic Dam Cu–U–Au–Ag–REE deposit, located in the Mesoproterozoic A-type granites of the Gawler Craton to the west of Arkaroola (Idnurm and Heinrich 1993).

Previous fluid inclusion studies from the Mt Painter Inlier

The Mt Painter Inlier is poorly studied compared to other Australian Proterozoic inliers, and the scarcity of fluid inclusion studies illustrates this point. Lottermoser (1987) and Teale and Lottermoser (1987) investigated the composition of Palaeozoic fluids in alkaline to peralkaline granites, associated pegmatites and breccias located to the west (Umberatana) of the presently studied veins, similar to the Pinnacles and Sitting Bull (see Fig. 1). The volatile-rich character of these intrusions is expressed by the late-stage growth of minerals such as fluorite, apatite and tourmaline in the metapelitic aureole, by the presence of pegmatites, and by large-scale breccias. The fluid inclusion study of Lottermoser (1987) revealed the presence of many types of fluids entrapped in early magmatic quartz and albite. Some inclusions contain up to eight different solid phases, which remained unidentified; other inclusions were highly saline with a halite cube. CO_2 was identified in another type of inclusion. The presence of fluid inclusions with an extremely large variation in salinity was suggested to have resulted from a transition from magmatic to saline hydrothermal conditions. This is the only work done on the Palaeozoic fluid evolution of the Mt Painter Inlier, and illustrates the profound lack of information available.

Diopside–titanite veins

One of the main goals of the present study is to understand the formation conditions of the enigmatic diopside–titanite veins (Fig. 2) as obtained from fluid and melt inclusions. Two theories may be put forward

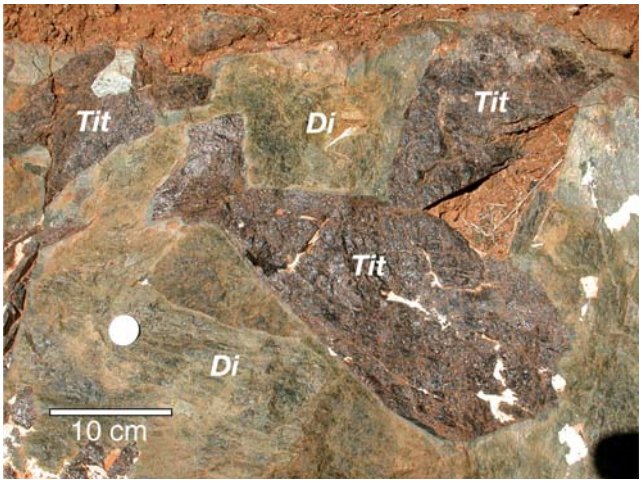

Fig. 2 Euhedral titanite (*Tit*) and diopside (*Di*) crystals in a vein from Radium Creek

for the vein origin, one involving a relationship with contemporaneous magmatism, and the other proposing a link with sedimentary calc-silicates. The main magmatic event in the area, dated around 440 Ma, was the intrusion of the I–S type British Empire Granite (Fig. 1), of which Nd isotope data point towards input of a mantle component (Elburg et al. 2003). A-type leucogranites and pegmatites have yielded older, Delamerian (498 ± 6 Ma) Sm–Nd ages (Elburg et al. 2003), although some doubt is cast upon these ages by the undeformed nature of these leucogranites (P.D. Bons, personal communication). The REE-rich chemistry of the studied diopside–titanite veins (see below) may in part be related to an agpaitic or a miaskitic igneous origin (e.g. Khomyakov 1995; Sørensen 1997; Arzamaststev et al. 2000; Bea et al. 2001). A long interval of crystallization is characteristic for agpaitic rock and may be combined with intervals of liquid immiscibility (e.g. Kogarko and Romanchev 1983). Methane-rich and other hydrocarbon gases were analysed in fluid inclusions in agpaitic rock (Konnerud-Madsen and Rose-Hansen 1982) in the Ilimaussaq complex (Greenland) illustrating the reduced environment of fluid entrapment. Late separation of sodium-rich fluid phases, by immiscibility or transition from low-temperature melt into hydrothermal fluids, caused late- and post-magmatic alteration of rock, e.g. albitization (see Sørensen 1997). However, there is no unequivocal evidence for contemporaneous alkaline magmatism in the Mt Painter Inlier, and the Nd isotopic signature of the veins indicate that they inherited their rare earth elements from the Mesoproterozoic A-type granites in the area (Elburg et al. 2003). Moreover, there has not been any report in literature about the association of diopside–titanite veins with agpaitic or miaskitic magmas, as associated pyroxenes in this case generally have a jadeitic or aegerine-augitic compositions (e.g. Khomyakov 1995).

As an alternative to igneous origin, metamorphism of sedimentary rocks is another process that may cause the formation of diopside (e.g. Winkler 1979; Tsujimori 1997). Reactions in siliceous dolomitic limestones (skarns) may produce diopside in addition to CO_2. Diopsidic clinopyroxenes may be formed in marls and mafic rock in the absence of CO_2 at high temperatures, and diopside is locally present in the metasedimentary Neoproterozoic rocks that cover the Mt Painter Inlier, i.e. at a structurally higher level than where the veins are found. Even in ultramafic rocks, addition of calcium may result in the formation of metamorphic diopside. Coarse-grained diopside crystals were reported by Wang and Williams (2001) that have grown in open-space veins during breccia and skarn development in metasedimentary and mafic metavolcanic host rock at Mt Elliott (NW Queensland, Australia). Diopside-rich veins may also have a hydrothermal origin (e.g. Magde et al. 1995), where the hydrothermal activity may be dominated by magmatic fluids.

Methods and techniques applied

Mineral paragenesis was determined by a petrographic study of the veins. Doubly polished thick- sections were then prepared from the diopside–titanite veins and hematite–quartz associations selected from the locations indicated in Fig. 1. A detailed description of the petrography and distribution of inclusions provided a framework for classification of mineralization and inclusions types. A Jobin Ivon LABRAM confocal-Raman spectrometer equipped with a frequency-doubled Nd-YAG laser (100 mW, 532.2 nm) with a LMPlanFI 100 × /0.80 objective lens (Olympus) was used to identify fluid and solid phases in inclusions. Diopside, titanite, apatite, wakefieldite (a rare earth element vanadate), actinolite and epidote were analysed with an ARL-SEMQ 30 electron microprobe equipped with four wavelength-dispersive spectrometers with TAP, LiF and PET diffraction crystals, and a LINK AN 10/25S energy-dispersive spectrometer (EDS). Beam conditions were 20 kV and 15 μA. Standards used for the microprobe analyses are natural kaersutite (*Al*, *Ca*, *Fe*, *K*, *Mg*, *Na*, *Si*), ilmenite (*Fe*, *Ti*), chromite (*Cr*), rhodonite (*Mn*), apatite (*Ca*, *P*), biotite (*K*), jadeite (*Na*), tugtupite (*Cl*), zircon (*Zr*), barite (*Ba*, *Sr*), arsenopyrite (*As*), metallic *V*, metallic *Nb*, and uraninite (*U*). Microprobe analyses for REEs in titanite, wakefieldite and epidote were calibrated with REE glass standards (Drake and Weill 1972), including REE1 (*Gd*, *Eu*), REE2 (*Nd*, *Sm*) and REE3 (*Ce*, *La*, *Pr*, *Y*). The detection limits of major elements and REEs are 0.02–0.11 and 0.08–0.13 mass%, respectively. Microthermometric measurements were carried out with a Linkam MDS 600 stage operating over a temperature range from –190 to +600°C. Synthetic fluid inclusions were used for the calibration at –56.6, 0.0 and 374.0°C. Volume fractions of vapour bubbles were obtained from area analysis in a two-dimensional projection of fluid inclusions (Bakker and Diamond 2006).

The computer package *FLUIDS* (Bakker 2003; Bakker and Brown 2003) was used to calculate fluid properties, including isochores, from (partial-) homogenization and melting/dissolution temperatures. All calculations were performed in the H_2O–NaCl fluid

system. Consequently, salinities are expressed in equivalent mass% NaCl. The program *Loner32* (Bakker 2003) is a modification of the H_2O–NaCl fluid system according to Bodnar and Vityk (1994) and was used to calculate salinities and isochores from both homogenization and melting temperatures. The program *AqSo1e* was used to calculate critical points and salinities at the *HLV* curve in the NaCl–H_2O system (Sterner et al. 1988), i.e. the dissolution of halite crystals in the presence of both liquid and vapour phases. Salinity estimations are slightly different from true values in fluid inclusions where the homogenization of liquid and vapour phases occurs before dissolution of the halite crystal, as the liquidus of the system is not independent of pressure (see Bodnar and Vityk 1994). This modification is taken into account in the program *Loner32*. The density and molar volume of the H_2O–NaCl fluid are obtained from the program *Loner15* (Anderko and Pitzer 1993). The properties of pure H_2O were calculated using the Haar et al. (1984) equation of state with the program *Loner14* (Bakker 2003).

Petrography and mineralogy of veins

Field observations

The diopside–titanite veins are up to 1.5 m wide and are hosted by Mesoproterozoic A-type granites (see also Elburg et al. 2003). They have a sharp angular contact with the host rock, and wall-rock interaction is not detected in outcrops. They consist of large, up to 60 cm long, often euhedral crystals of diopside with or without euhedral crystals of titanite, up to 40 cm long (Fig. 2). Most commonly, diopside comprises 90% of the volume of the veins and titanite 10% with minor quartz and magnetite. The contact between diopside and titanite is approximately along rational faces of both minerals, without any trace of corrosion or reactions. Both diopside and titanite, therefore, belong to the same crystallization event, and appear to have grown in open space. Diopside–titanite veins have a laterally limited occurrence, and may be overprinted by a similarly orientated quartz–hematite veining system. The titanite–diopside veins are sometimes spatially associated with granitic pegmatites. At the contact, graphic intergrowths of diopside and feldspar are observed.

The quartz–hematite mineral assemblages have a variable appearance, and may occur in regular veins or in complex brecciated zones between fragments of the host rock (Fig. 3). The breccias consist of reddish hematite-altered metasedimentary and granitic fragments (Fig. 3a), cemented by coarse quartz. At present, open spaces still occur between the cements in the veins, revealing bundles of euhedral quartz crystals. Brecciated zones are up to 1.5 m wide and may have a spotted appearance, consisting of dark concretions of hematite, which are overgrown by bright quartz. Discrete veins with a similar mineralogy are associated

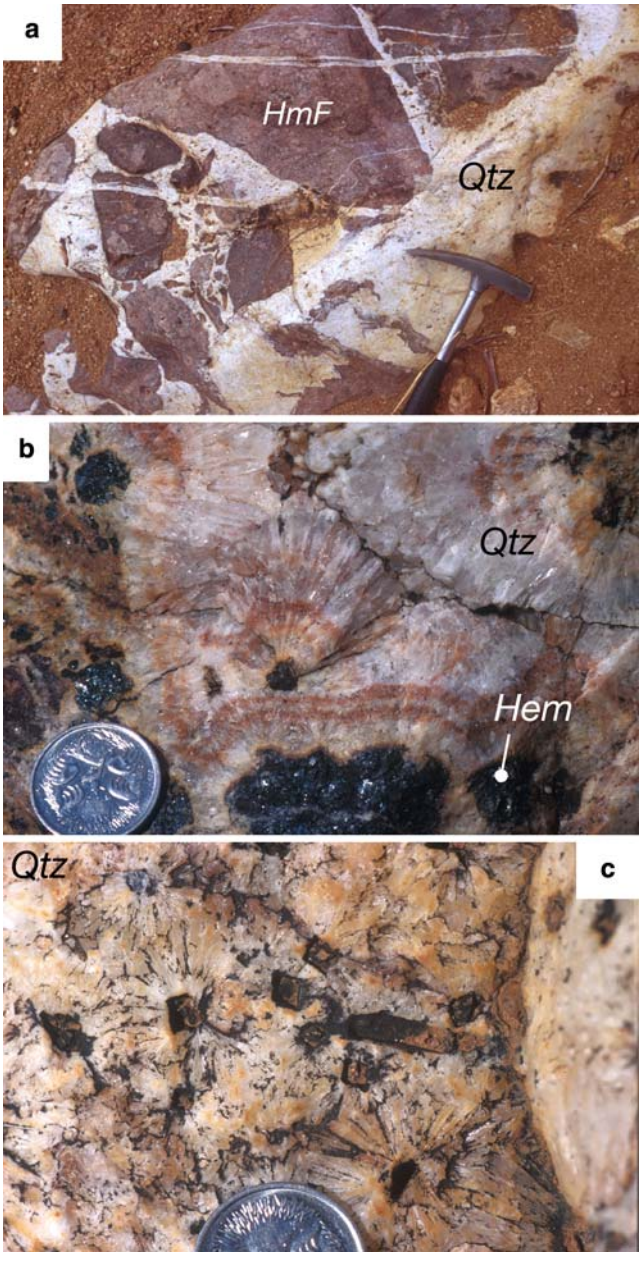

Fig. 3 **a** Brecciated hematitized host rock (*HmF*) cemented with quartz from Mt Gee. **b** Spotted vein consisting of hematite concretions in quartz and host rock. Concentrically and radially grown quartz at hematite concretions. **c** Rhombohedral nailholes (remnants of unknown altered minerals) in the centre of bundles of quartz. The illustrated coin has a diameter of 24 mm

with the breccias. Within these veins, fragments of the host rock have been intensely hematitized, as reflected by its reddish colour. The vein quartz grew concentrically and radially around hematite concretions (Fig. 3b) and around thick needle-shaped single crystals with a rhombohedral cross section (Fig. 3c), often ending in bundles of coarsely grown euhedral quartz crystals. The original, thick needle-shaped crystals are completely altered or dissolved and cannot be identified.

Minor amounts of fluorite were observed, associated with the quartz–hematite veins and breccias. Locally, the fluorite is present in euhedral cubic crystals with sizes up to 3 cm in length. Zonation in the fluorite is obvious from its banded colour variation: from green in the core of fragments to an alternation of white and purple (locally up to black) in the rims. Similar to quartz, fluorite also grew concentrically and radially. Furthermore, fluorite alternates with thin zones of quartz (up to 1 mm thickness), illustrating the contemporaneous nature of both mineralizations. Locally, the outer surface of fluorite is corroded and overgrown by massive quartz–hematite. Fluorite has not been observed in or near the diopside–titanite veins.

The diopside–titanite veins are locally affected by the quartz–hematite mineralization event (Fig. 4). Brecciated fragments of single titanite and diopside crystals are overgrown by quartz (Fig. 4a). Diopside crystals show strong hematite-rich alteration zones along brecciated parts, reflected by a reddish rim (Fig. 4b). The titanite does not show any signs of overprinting by hematite. Locally, bladed calcite is observed, which has grown directly onto diopside surfaces (Fig. 4c). Bundles of coarsely grown quartz, similar to pure quartz–hematite mineralization, have subsequently grown concentrically and radially around this calcite.

Microscopic observations and microprobe analyses of diopside–titanite veins

Diopside and titanite crystals are internally undeformed, apart from the presence of some cracks, which are occasionally healed. Diopside has been locally replaced by massive actinolite, which has a slightly darker-green appearance. The diopside has a relatively homogeneous composition of $En_{38.9–44.3}Fs_{7.0–12.3}Wo_{46.6–49.5}$ (Table 1). Zonation is not observed and the diopside does not contain any REEs. The diopside has a well-defined Raman spectrum with the main peaks at the relative wavenumbers 326, 392, 669 and 1,015 cm^{-1}. The intensity of the individual peaks is nearly independent of the orientation of the crystals relative to the laser-beam polarization.

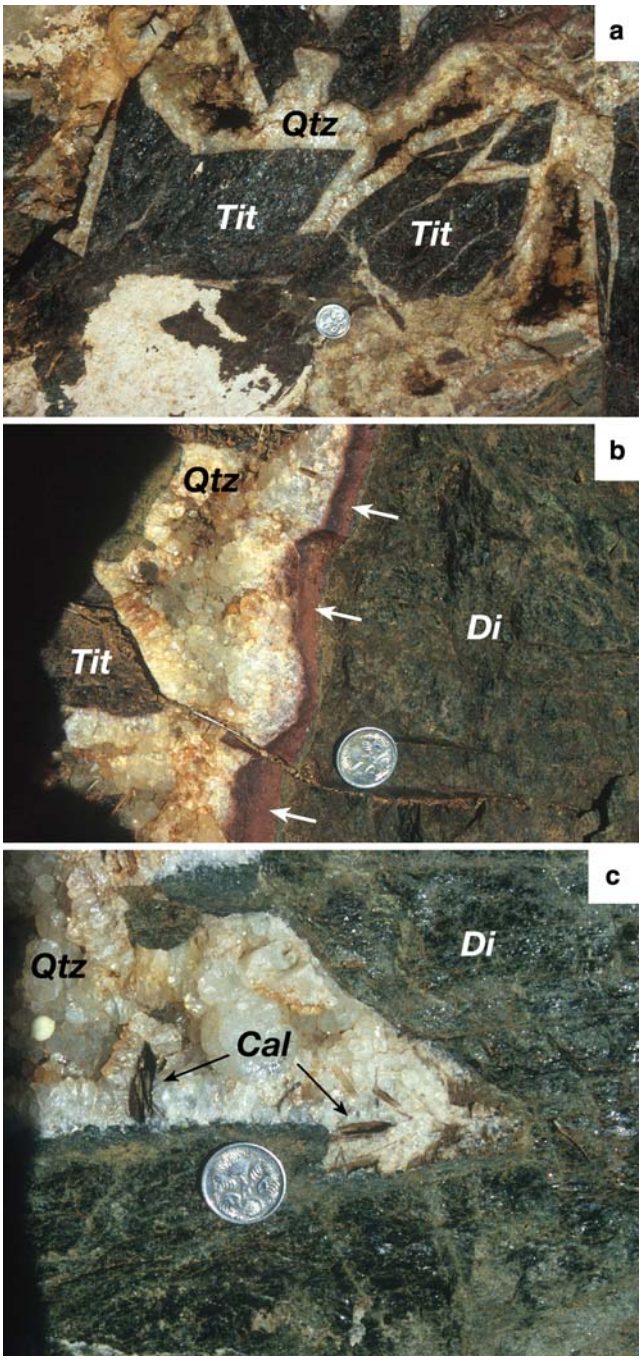

Fig. 4 **a** Brecciated titanite crystals overgrown by quartz of the second generation. **b** Fragment of titanite and diopside, also overgrown by the late quartz generation. The rim of the diopside is altered to a reddish agglomerate of minerals (mainly hematite, *arrows*). **c** Quartz is precipitated concentrically around a bladed calcite crystal, grown at a diopside fragment. The illustrated coin has a diameter of 24 mm

Titanite locally has an irregular zonation pattern near to its rims (Fig. 5), reflecting two different stages

Table 1 Range in results from electron microprobe analyses of titanite and diopside

	Titanite (dark) $n = 9$	Titanite (bright) $n = 7$	Diopside $n = 9$
SiO_2	29.70–30.74	30.10–30.76	52.99–55.46
TiO_2	35.07–35.49	33.05–33.14	–
Al_2O_3	0.51–0.85	0.81–0.98	0.18–0.29
Cr_2O_3	0.00–0.13	0.00–0.08	0.00–0.08
Y_2O_3	1.12–1.54	2.49–3.12	–
La_2O_3	0.00–0.17	0.17–0.33	–
Ce_2O_3	0.55–0.77	0.87–1.03	0.00–0.06
Pr_2O_3	0.63–0.70	0.51–0.78	0.00–0.06
Nd_2O_3	0.59–0.97	1.06–1.38	–
Sm_2O_3	0.15–0.21	0.20–0.36	–
Eu_2O_3	0.00–0.09	–	–
Gd_2O_3	0.27–0.31	0.28–0.44	0.00–0.04
FeO	1.89–2.44	2.98–3.41	6.59–9.83
MnO	–	0.02–0.06	0.09–0.78
NiO	0.00–0.13	–	0.00–0.07
MgO	0.00–0.09	0.09–0.13	12.91–13.41
CaO	25.12–25.5	23.14–24.9	21.44–26.68
Na_2O	0.06–0.18	0.00–0.18	0.41–0.89
P_2O_5	0.06–0.09	0.00–0.12	0.00–0.05
Total	97.55–99.33	97.82–99.39	97.74–99.68

Values given in mass%

of crystal growth or possibly leaching. ''Bright'' titanite occurs near the rim, and is slightly depleted in Ti and Ca compared to the bulk, ''dark'' titanite, which is slightly enriched in Fe and Al (Tables 1, 2). Microprobe analyses also illustrate that the ''bright'' titanite is significantly enriched in REEs, containing

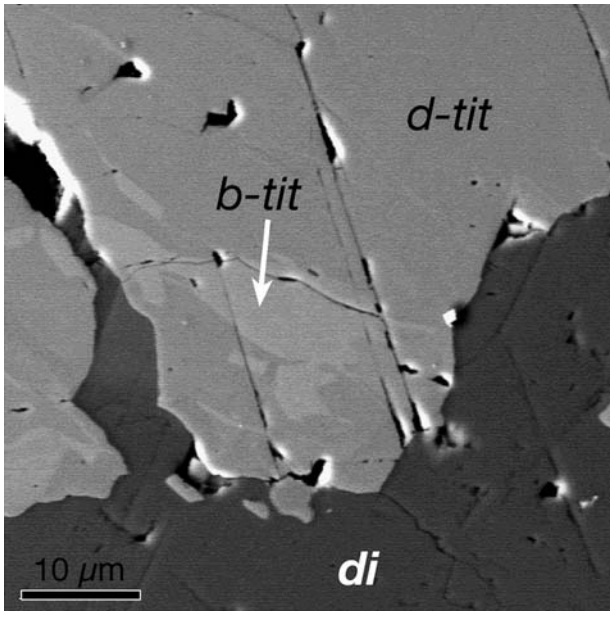

Fig. 5 Back-scattered electron image of titanite, illustrating zonations in titanite. *b-tit* and *d-tit* are relatively bright and dark titanite, respectively. *di* diopside. See text for further details

Table 2 Number of ions in the titanite from Table 1 on the basis of four silicium. Iron is recalculated as Fe_2O_3

	Titanite (dark) $n = 9$	Titanite (bright) $n = 7$
Si	4.000	4.000
Al	0.078–0.135	0.124–0.187
Fe^{3+}	0.192–0.270	0.326–0.461
Cr	0.000–0.013	0.000–0.082
Ti	3.419–3.643	3.120–3.304
Mg	0.000–0.017	0.000–0.025
Mn	–	0.002–0.007
Ni	0.000–0.014	–
Na	0.008–0.045	0.000–0.045
Y	0.075–0.115	0.172–0.221
REE	0.101–0.133	0.148–0.166
Ca	3.497–3.716	3.140–3.545
O	19.64–20.07	19.53–20.00

REE includes La, Ce, Pr, Nd, Sm, Eu and Gd

up to 7.5 mass% Y_2O_3 and REE_2O_3 (Table 1), of which Nd_2O_3 and Ce_2O_3 are the most abundant (1.4 and 1.0 mass%, respectively). The ''dark'' titanite contains no more than 4.8 mass% REE_2O_3. EDS analysis within titanite revealed an unknown Nb–Y phase, perhaps similar to euxinite-(Y), which might link the diopside–titanite veins with the previously mentioned primary pegmatite-related uranium mineralizations.

The diopside–titanite veins belong to a chemically completely different system than granitic pegmatites. As mentioned before, crosscutting or intergrowth of both systems is observed in the field, revealing a graphic texture of coarse-grained diopside in albite.

Table 3 Individual electron microprobe analyses of the zoned calcic amphibole

	nr. 20	nr. 25	nr. 24	nr. 23	nr. 21
SiO_2	58.09	56.63	55.83	55.64	56.71
TiO_2	–	–	0.02	–	–
Al_2O_3	0.26	0.77	0.47	0.26	–
La_2O_3	–	0.03	0.03	–	–
Ce_2O_3	0.03	0.03	–	0.03	0.06
Pr_2O_3	0.05	–	–	0.03	0.07
Nd_2O_3	–	0.03	–	–	–
Sm_2O_3	–	–	0.03	–	–
Eu_2O_3	0.10	–	0.10	–	0.06
Gd_2O_3	–	–	–	–	–
FeO	8.35	9.48	10.79	10.71	5.22
MnO	0.77	0.95	1.34	4.75	10.66
MgO	18.24	16.00	15.44	13.35	13.09
CaO	14.73	14.23	14.53	14.06	13.90
Na_2O	0.14	0.04	0.05	0.05	0.30
K_2O	0.06	0.04	0.04	0.01	0.22
Total	100.82	98.38	98.67	98.89	100.29

Values given in mass%

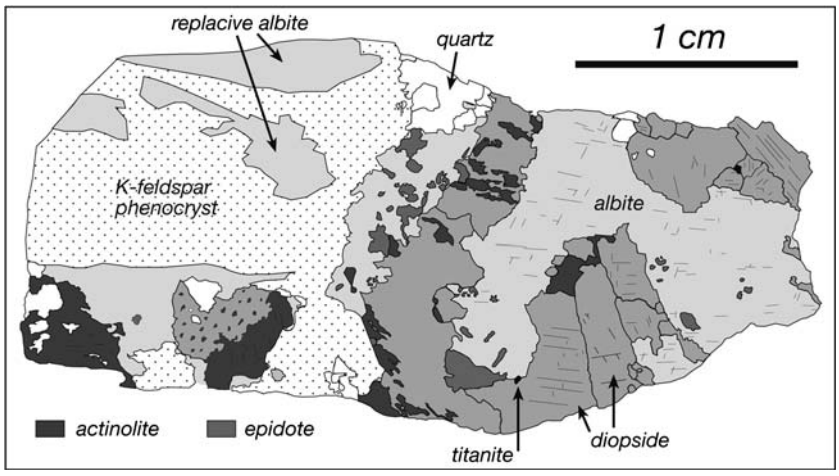

Fig. 6 Schematic drawing of a thin section with graphic intergrowth of diopside and albite, in contact with K-feldspar phenocryst in the granitic pegmatite

Microscopic petrography reveals a strong albitization of K-feldspar phenocrysts in the granitic pegmatite (Fig. 6) at the contact with diopside–titanite veins. Minor amounts of quartz, epidote and titanite are present. Diopside is strongly affected by amphibole alteration. The combined mineralization of diopside and albite occurs only at the contact with granitic pegmatites. It is unclear whether these two minerals co-crystallized, or the diopside overprinted the granitic pegmatite. In view of the virtually alumina-free nature of the diopside–titanite association, the latter option appears more plausible.

Microscopic observations of quartz–hematite veins and fluorite

Quartz in the quartz–hematite mineralization has abundant Brazil twins, mainly visible in sections parallel to the *c*-axis (Fig. 7). The twins are also marked by different amounts of fluid inclusions. Locally, zones may contain high concentrations of irregular fluid inclusions, which are not always present along the entire zone. Other zones contain many tiny inclusions, giving the quartz a cloudy appearance (*fi.c* in Fig. 7). These zones alternate with inclusion-free zones. Relicts of magnetite occur in hematite-rich veins and have been systematically replaced along cracks and cleavage planes by hematite. In reflected light, two different types of hematite are observed, based on slight differences in reflectivity. Fluorite exhibits oscillatory zoning with bands of a variety of purple colours on top of cores of green fluorite. Locally, haloes of black to deep-purple coloured fluorite (radiation damage) occur around enclosed unidentified dark grains. EDS spectra of the fluorite reveal small peaks for Sr, Y and LREE.

Intermediate assemblage

Microscopic investigations revealed the presence of fine-grained amphibole needles, epidote, apatite and wakefieldite at the interface between diopside–titanite and quartz–hematite associations (Fig. 8). The amphibole needles have a different appearance from the previously mentioned alteration of diopside into massive actinolite. Amphibole needles have grown on diopside surfaces and have partly replaced diopside, but also extend for several millimetres into the subsequently overgrowing quartz and calcite (Fig. 8a, d). The amphibole needles have been identified as actinolite (Tables 3, 4) and are zoned with respect to Mn, Mg and Fe. Locally, the Mn content reaches 10.7 mass% MnO, which is exceptionally high for actinolite. None of the actinolite contains significant amounts of REEs. Epidote also appears as an

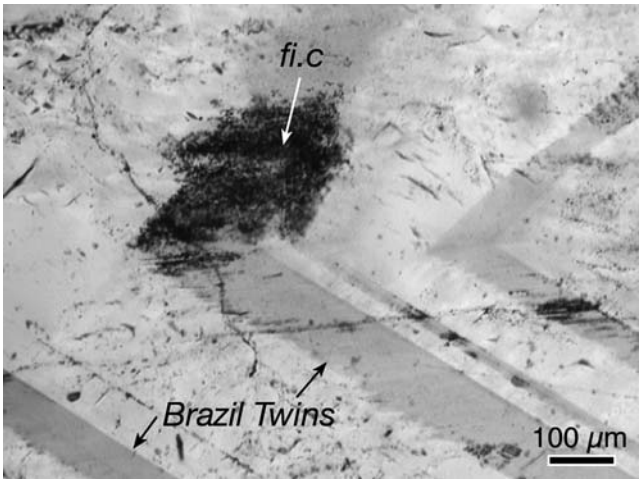

Fig. 7 Brazil twins in the second quartz generation in crossed polarized light, partly marked by clouds of fluid inclusions

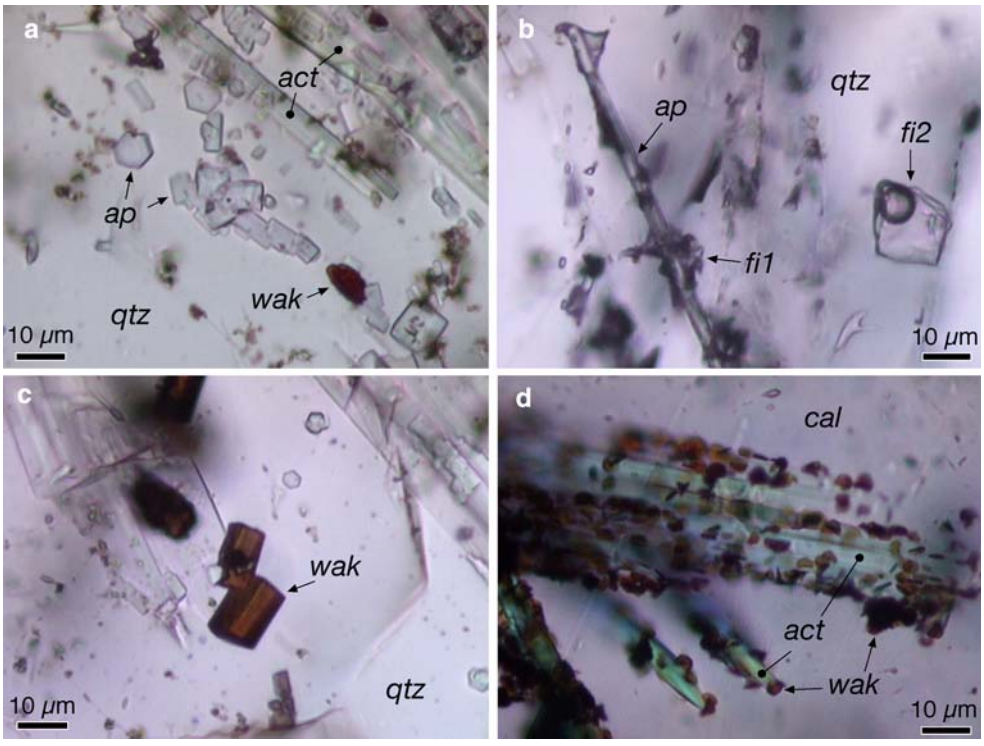

Fig. 8 Microphotographs of **a** Actinolite needles (*act*), apatite (*ap*) and wakefieldite (*wak*) crystals in quartz (*qtz*); **b** Apatite needle in quartz with pinned fluid inclusions (*fi1*) in addition to a two-phase fluid inclusion (*fi2*) within the quartz; **c** Euhedral wakefieldite crystals in quartz; **d** Wakefieldite crystals pinned to actinolite needles in calcite (*cal*)

alteration product of diopside. It is dominantly $FeAl_2$-epidote but has thin zones and patches of REE-rich epidote (allanite) (Tables 5, 6). The allanite contains up to 19 mass% REE_2O_3, mainly Ce_2O_3 (9.6 mass%), La_2O_3 (3.9 mass%) and Nd_2O_3 (3.4 mass%), but Y_2O_3 is effectively absent. Apart from normal euhedral growth zones, more irregular patches of allanite are present (resembling turbulent flow patterns) within the epidote cores and are inferred to reflect a secondary injection of extremely REE-enriched fluids along cracks, resulting in alteration of the already crystallized $FeAl_2$-epidote core. Small euhedral crystals of apatite (hexagonal shape) are attached to actinolite needles (Fig. 8a) and are enclosed by quartz (Fig. 8b). Apatite also crystallized as long needles, which have partly pinned fluid inclusions during the later stage of quartz growth (*fi1* in Fig. 8b). Numerous reddish-brown prismatic euhedral crystals of wakefieldite (REE-rich vanadate), up to 10 μm in length, are pinned to both actinolite and apatite needles (Fig. 8c, d). Ce, Nd, La and Gd are the major REEs in this vanadate mineral (Table 7). Individual wakefieldite grains contain variable amounts of arsenate in the major anion complex, i.e. from 4.2 to 19.0 mol% in $(V,As)O_4^{3-}$ (compare analysis nr. 10 with nr. 12 in Table 8, respectively). The mineral formula varies between $(Ce_{0.34}Y_{0.11}Nd_{0.30}La_{0.08}Gd_{0.08}Sm_{0.05}Eu_{0.03})(V_{0.82}As_{0.19})O_4$ and $(Ce_{0.48}Y_{0.0}Nd_{0.29}La_{0.10}Gd_{0.06}Sm_{0.03}Eu_{0.02})(V_{0.96}As_{0.04})O_4$. A coupled decrease in Ce and increase in Y corresponds to an increase in As, whereas other REEs (e.g. Nd, La, Gd, Sm and Eu) remain nearly constant. The deficiency in the total of microprobe analyses (Table 7) is due to the fact that not all REEs were determined. The Raman spectra corresponding to the analysed wakefieldite crystals are illustrated in the Appendix (Fig. 26).

Table 4 Number of ions for the amphiboles in Table 3 on the basis of 23 oxygens anhydrous

	nr. 20	nr. 25	nr. 24	nr. 23	nr. 21
Si	7.976	8.012	7.955	8.010	8.064
Al	0.024	–	0.045	–	–
Al	0.018	0.128	0.034	0.044	–
Ti	–	–	0.002	–	–
Mg	3.733	3.375	3.280	2.865	2.775
Mn	0.090	0.114	0.162	0.579	1.284
Fe^{2+}	0.959	1.122	1.286	1.289	0.621
REE	0.009	0.005	0.008	0.003	0.010
Na	0.037	0.011	0.014	0.014	0.083
Ca	2.167	2.157	2.218	2.169	2.118
K	0.011	0.007	0.007	0.002	0.040
OH	2.00	2.00	2.00	2.00	2.00
Mg[a]	78.0%	73.2%	69.4%	60.5%	59.3%
Fe[a]	20.1%	24.3%	27.2%	27.3%	13.3%
Mn[a]	1.9%	2.5%	3.4%	12.2%	27.4%

REE includes La, Ce, Pr, Nd, Sm, Eu and Gd

[a]Mole percentage Mg/(Mg + Fe + Mn), Fe/(Mg + Fe + Mn) and Mn/(Mg + Fe + Mn)

Table 5 Individual electron microprobe analyses of the zoned epidote, ordered according to mass% of Ce_2O_3

	nr. 27	nr. 30	nr. 24	nr. 37	nr. 33	nr. 28	nr. 26	nr. 31	nr. 29	nr. 23	nr. 25
SiO_2	37.47	37.80	37.38	37.97	36.26	37.48	34.86	34.13	33.81	33.31	33.88
TiO_2	0.09	0.04	0.01	0.01	–	0.04	–	0.06	–	0.01	–
Al_2O_3	18.73	19.37	18.58	20.02	18.92	15.90	15.85	12.44	10.99	11.95	11.75
Fe_2O_3	16.53	17.39	17.00	13.56	15.22	12.60	15.67	13.34	14.21	11.58	10.56
Y_2O_3	0.56	0.42	0.28	0.64	0.48	–	0.07	–	0.13	0.06	–
La_2O_3	0.03	–	0.11	0.16	0.51	1.85	1.82	3.03	3.39	3.23	3.94
Ce_2O_3	0.10	0.13	0.2	0.33	1.35	4.30	4.36	7.93	8.45	8.90	9.59
Pr_2O_3	–	–	–	–	–	–	–	–	–	–	–
Nd_2O_3	0.21	0.14	0.14	0.31	1.09	1.74	1.64	3.42	3.46	3.61	3.43
Sm_2O_3	0.08	0.08	0.06	–	0.30	0.19	0.24	0.35	0.43	0.40	0.51
Eu_2O_3	0.10	–	–	–	0.10	0.13	0.23	0.32	0.32	0.32	0.32
Gd_2O_3	0.13	0.13	0.03	0.15	0.46	0.63	0.63	1.07	1.17	1.22	1.29
FeO	1.91	1.18	1.33	3.40	1.78	6.98	4.17	9.15	9.22	10.28	10.28
MnO	0.08	0.13	0.08	0.18	0.23	0.10	0.14	0.24	0.25	0.20	0.20
MgO	0.10	0.10	–	–	0.19	–	0.21	0.06	0.12	0.24	0.24
CaO	22.39	23.03	22.89	21.24	20.99	18.69	18.56	14.23	13.49	12.89	13.31
SrO	–	–	–	0.44	–	–	–	0.47	1.41	–	–
Na_2O	–	–	–	–	0.07	–	–	–	–	–	–
K_2O	–	–	–	0.01	–	0.01	0.01	0.03	–	–	–
Total	98.51	99.94	98.09	98.42	97.95	100.64	98.46	100.27	100.85	98.20	99.30

Values given in mass%. Fe_2O_3 and FeO are corrected according to the formula of Droop (1987)

Table 6 Number of ions for the epidotes in Table 5 on the basis of 12.5 oxygen

	nr. 27	nr. 30	nr. 24	nr. 37	nr. 33	nr. 28	nr. 26	nr. 31	nr. 29	nr. 23	nr. 25
Si	3.052	3.028	3.053	3.088	3.019	3.163	3.023	3.100	3.110	3.121	3.156
Al	1.798	1.829	1.789	1.919	1.856	1.582	1.620	1.332	1.191	1.320	1.290
Fe^{3+}	1.013	1.048	1.045	0.830	0.953	0.800	1.023	0.912	0.984	0.817	0.740
Ti	0.006	0.002	0.001	0.001	0.002	0.003	–	0.004	–	0.001	–
Mg	0.012	0.012	–	–	0.024	–	0.027	0.008	0.016	0.034	0.033
Fe^{2+}	0.130	0.079	0.091	0.231	0.124	0.493	0.302	0.695	0.709	0.806	0.801
Mn^{2+}	0.006	0.009	0.005	0.012	0.016	0.007	0.010	0.018	0.019	0.016	0.016
Ca	1.954	1.977	2.003	1.851	1.872	1.690	1.725	1.385	1.329	1.294	1.328
REE	0.043	0.031	0.028	0.055	0.135	0.270	0.283	0.529	0.579	0.602	0.643

REE includes La, Ce, Pr, Nd, Sm, Eu and Gd

Table 7 Individual electron microprobe analyses of wakefieldite

	nr. 12	nr. 22	nr. 19	nr. 6	nr. 13	nr. 4	nr. 11	nr. 16	nr. 14	nr. 7	nr. 15	nr. 10
$V_2O_5^a$	26.32	26.43	27.83	27.40	29.72	28.84	29.45	26.27	30.07	31.10	30.45	30.98
$As_2O_5^a$	7.75	7.34	6.42	6.37	5.90	5.87	4.91	4.39	4.12	2.95	2.07	1.72
Y_2O_3	4.33	4.27	3.23	3.63	1.92	2.60	0.75	2.49	1.01	0.65	0.45	–
La_2O_3	4.68	4.27	5.74	5.16	6.02	5.26	5.22	4.61	4.92	3.41	4.15	5.83
Ce_2O_3	19.90	21.89	21.28	20.76	24.57	22.87	25.76	22.27	24.91	24.93	24.77	28.01
Nd_2O_3	17.75	16.85	16.82	17.77	18.93	17.34	19.33	19.09	20.10	22.37	21.35	17.37
Sm_2O_3	3.35	3.14	3.16	3.14	3.27	3.10	2.26	2.82	2.65	2.58	2.41	2.13
Eu_2O_3	1.71	1.57	1.29	1.14	1.48	1.29	1.39	1.53	1.63	1.57	1.53	1.49
Gd_2O_3	5.00	5.41	4.89	5.20	4.93	4.67	4.33	5.11	4.29	4.16	4.34	3.93
Total	90.79	91.17	90.66	90.57	96.74	91.84	93.41	91.58	93.70	93.72	91.51	91.46

Values in mass%. Minor amounts of P_2O_5 (0.29–3.24 mass%) and Cl (0.07–0.15 mass%) have been detected. Pb, Fe, Si, Sr and Ti are below detection limit. The signal is occasionally contaminated from the surrounding calcite (up to 3.47 mass% CaO)

[a]Recalculated values from V_2O_3 and As_2O_3 analyses

Table 8 Number of ions for the wakefieldite in Table 7 on the basis of four oxygen

	nr. 12	nr. 22	nr. 19	nr. 6	nr. 13	nr. 4	nr. 11	nr. 16	nr. 14	nr. 7	nr. 15	nr. 10
V	0.817	0.820	0.860	0.851	0.871	0.878	0.894	0.901	0.910	0.939	0.948	0.962
As	0.190	0.180	0.157	0.157	0.137	0.141	0.118	0.107	0.099	0.071	0.051	0.042
Sum	1.007	1.000	1.017	1.008	1.008	1.020	1.012	1.008	1.008	1.010	0.999	1.004
Y	0.108	0.107	0.080	0.091	0.045	0.064	0.018	0.062	0.025	0.016	0.011	–
La	0.081	0.074	0.099	0.090	0.098	0.089	0.088	0.079	0.083	0.057	0.072	0.101
Ce	0.342	0.376	0.364	0.357	0.399	0.386	0.433	0.380	0.418	0.417	0.427	0.482
Nd	0.298	0.283	0.281	0.298	0.300	0.285	0.317	0.318	0.329	0.365	0.359	0.291
Sm	0.054	0.051	0.051	0.051	0.050	0.049	0.036	0.045	0.042	0.041	0.039	0.034
Eu	0.027	0.025	0.021	0.018	0.022	0.020	0.022	0.024	0.025	0.025	0.025	0.024
Gd	0.078	0.084	0.076	0.081	0.072	0.071	0.066	0.079	0.065	0.063	0.068	0.061
Sum	0.989	1.000	0.972	0.987	0.987	0.964	0.980	0.987	0.986	0.984	1.002	0.994

Fluid and melt inclusions in vein minerals

Droplets of melt can be included in small pockets within newly formed minerals during crystallization in the magmatic stage of igneous rocks (e.g. Frezzotti 2001; Anderson 2003). These *primary* inclusions can be preserved in a glassy state (e.g. in volcanic rock) or may devitrify, react or recrystallize to a mineral assemblage that corresponds to the ambient bulk mother melt composition. In a late magmatic stage, volatiles and incompatible elements are concentrated in rest-melts, which may contain considerable amounts of a separated fluid phase (e.g. Thompson 1995). In this stage, both rest-melt and fluid may be entrapped in newly formed minerals (*primary* inclusions) or in cracks in early-formed igneous crystals (*secondary* inclusions). After complete crystallization of the magma, only fluids that may be enriched in salts and other incompatible materials remain, and may circulate in hydrothermal convection cells. In this stage, the system has proceeded to a pure hydrothermal stage. Again, these fluids may be entrapped as *primary* inclusions in newly grown minerals in veins, pores and vugs, or as *secondary* inclusions in cracks in minerals that are already present at the time the hydrothermal system was fully established. If more than two inclusion generations are recognized in single grains, *tertiary* and *quaternary* can also been used to indicate successive generations of ''secondary'' inclusions (i.e. inclusions in healed cracks). In our study, the relationship between inclusions and vein minerals, sequence of mineralization, heterogeneity and relative trapping temperatures of the fluids, as described in the following paragraphs, are summarized in Fig. 9.

Diopside

Two inclusion generations are present in fresh, uncorroded *diopside*: (1) Primary (heterogeneous, both melt and fluid inclusions), and (2) Secondary (homogeneous, halite-saturated fluid inclusions).

Primary inclusions occur in growth zones and clusters within *diopside* crystals (Fig. 10). Growth zones contain regular inclusions with an elongate

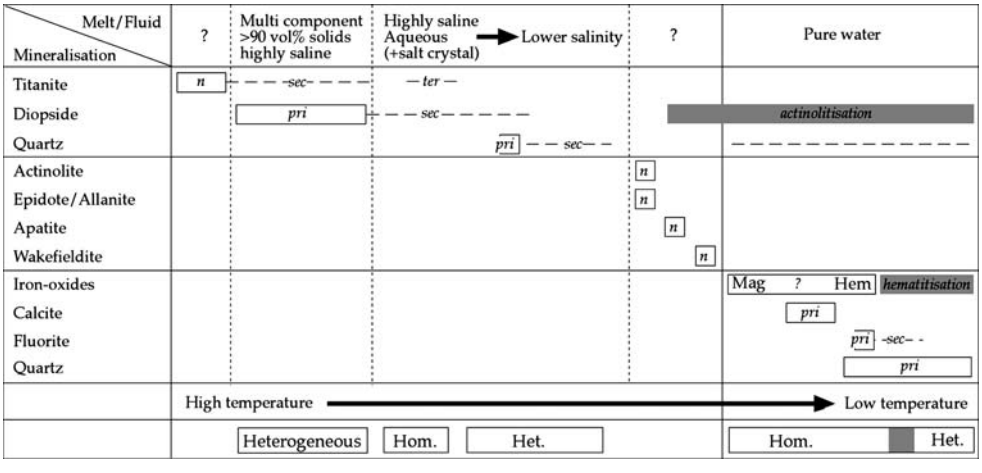

Fig. 9 Relationship between mineralizations and fluids involved in both the pegmatitic stage and the hydrothermal stage. The *boxes* indicate relative timing of crystallizations. *n* no fluid or melt included, *pri* primary inclusions, *sec* secondary inclusions, *ter* tertiary inclusions. The immiscibility of the fluid is indicated with heterogeneous (or *Het.*) and homogeneous (or *Hom.*). See text for further details

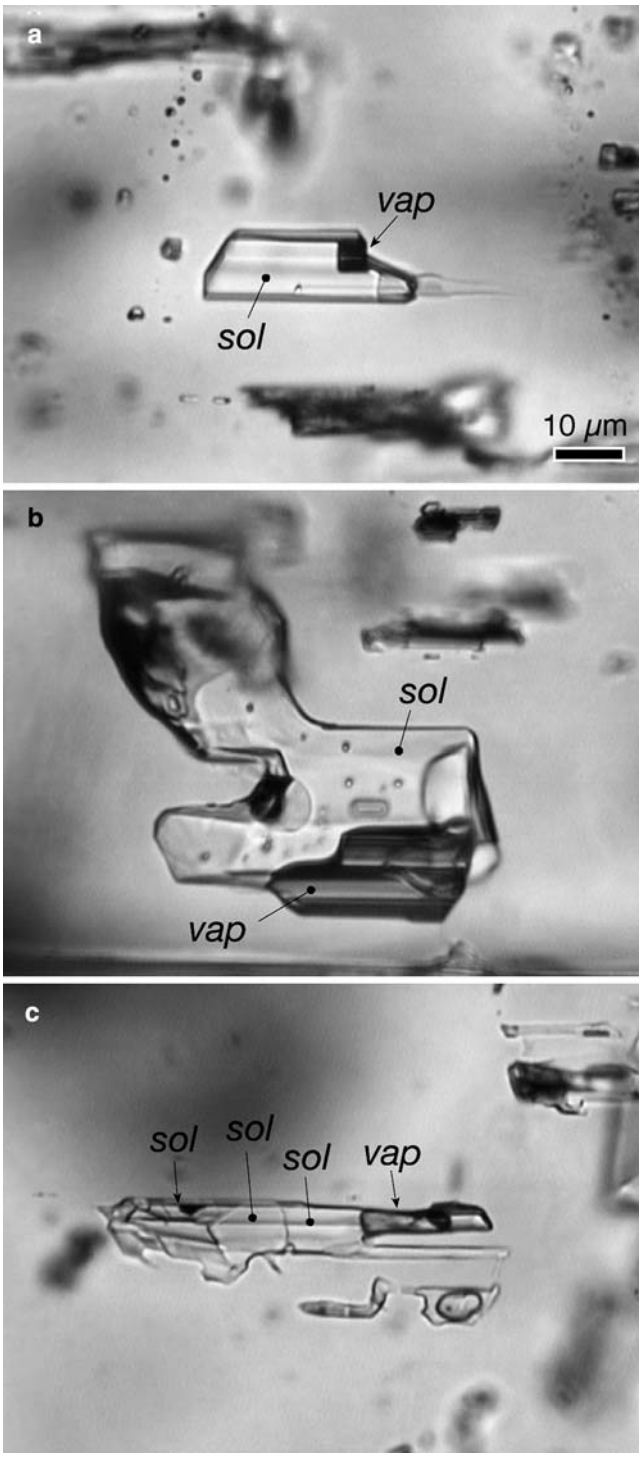

Fig. 10 Examples of primary fluid/melt inclusions in diopside. *vap* water vapour bubble, *sol* solid (including numerous distinctive phases). See text for further details

(negative crystal) shape, up to 20 μm long, whereas clusters have large irregularly shaped inclusions (up to 100 μm), but their walls are commonly defined by rational faces of the host mineral. Both types of inclusions contain variable amounts of solid phases (up to 90 vol.%), a vapour bubble (usually deformed) and a highly saline aqueous solution (varying between 0 and 10 vol.%), reflecting highly heterogeneous fluid/melt trapping conditions (Fig. 9). The distribution of the solid phases among the inclusions is highly variable; some contain only one or two transparent solids (Fig. 10a), whereas others display a variety of crystals (Fig. 10b, c) of which some are birefringent and some are opaque. These inclusions are considered recrystallized glass inclusions, i.e. relicts of melt during crystallization of *diopside*, which contain variable amounts of hyper-saline aqueous solution (EDS analyses reveal the presence of Cl, Na and K). Raman spectra of the solid phases within these inclusions demonstrate that calcite, anhydrite, magnetite and several unknown minerals are present (see Appendix, Fig. 27). However, some of the included solids, probably salts, are Raman inactive. A vapour bubble, usually deformed as it is squeezed between the enclosed crystals, is present in all inclusions, whereas the presence of a liquid phase could not always be confirmed. Gases like CO_2, CH_4, N_2, O_2 and H_2 were not detected by Raman microspectrometry in the vapour bubble, which most probably consists of water vapour. Salt-rich inclusions' microthermometry (e.g. Fig. 10c) reveals salt melting temperatures commonly up to 508°C

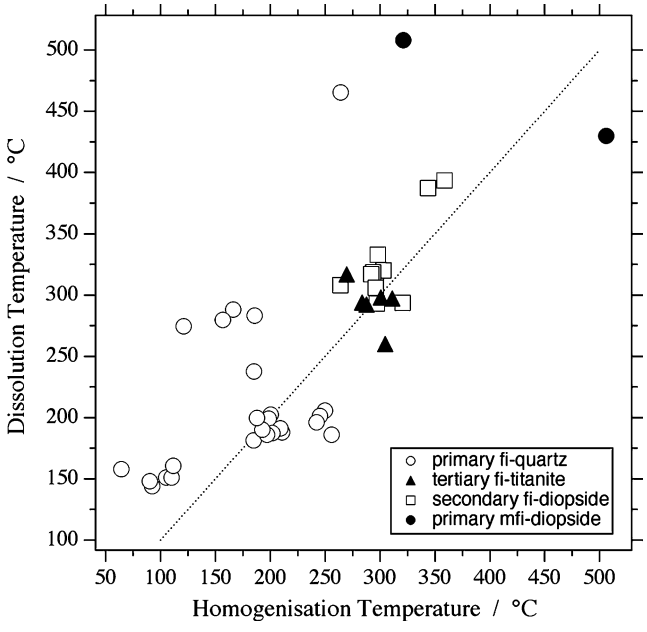

Fig. 11 Diagram of homogenization temperature ($L + V \Rightarrow L$) versus dissolution temperatures of halite ($S + L \Rightarrow L$) for fluid inclusions in diopside, titanite and associated quartz. See text for further details

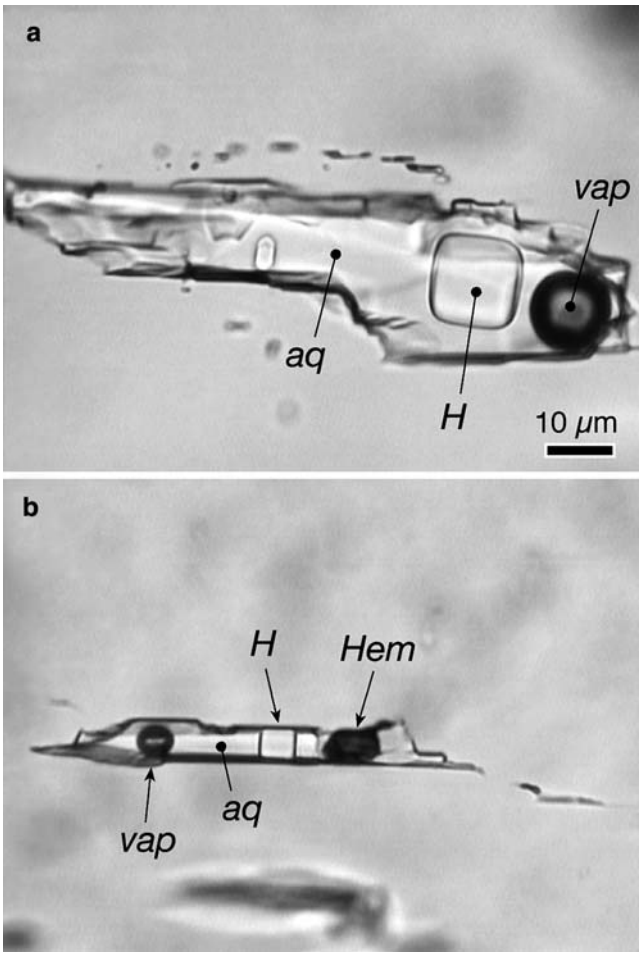

Fig. 12 Examples of secondary fluid inclusions in diopside. *H* halite cube, *Hem* hematite, *vap* vapour, *aq* saline aqueous solution. See text for further details

(*primary mfi-diopside* in Fig. 11), locally exceeding 600°C (the limit of the heating–freezing stage), and homogenization temperatures ($L + V \Rightarrow L$) up to 578°C. Total homogenization, including all solid phases present in the inclusions, did not occur below 600°C. Most inclusions decrepitated below this temperature. Salinities up to 61 eq. mass% NaCl are calculated, but higher salinities are indicated by melting temperatures exceeding 600°C.

The secondary inclusions in *diopside* lie along curved trails (healed cracks) that locally crosscut grain boundaries. These inclusions have a flat and irregular shape, with sizes up to 100 μm in diameter (Fig. 12). They contain a saline fluid with a vapour bubble (7–10 vol.%) and a salt cube (9–14 vol.%), reflecting a relatively homogeneous fluid (Fig. 9). Hematite is typically absent in most inclusions (Fig. 12a) but constitutes up to 11 vol.% in some inclusions (Fig. 12b), and is thus believed to have been trapped accidentally. Apart from the hematite, most of these fluid inclusions appear to have similar bulk compositions and molar volumes. Homogenization temperatures of the fluid phase, i.e. $L + V \Rightarrow L$, occur mainly between 290 and 310°C (Figs. 11, 13a). The dissolution temperature of the halite crystal varies between 293 and 333°C, illustrating slight variation in salinity (*secondary fi-diopside* in Fig. 11). In general, dissolution temperatures are higher than liquid–vapour homogenization temperatures. Calculated salinities range from 38.7 to 41.2 eq. mass% NaCl. Calculated molar volumes range from 22.3 to 22.7 $cm^3\ mol^{-1}$. Only some inclusions have a composition intermediate between the primary and secondary inclusions, indicated by higher homogenization temperatures, up to 359°C (Fig. 13a), and higher salinities, with T_M up to 394°C. These temperatures correspond to a salinity of 46–47 eq. mass% NaCl and molar volumes up to 23.6 $cm^3\ mol^{-1}$.

Titanite

Three generations of inclusions are observed in *titanite*: (1) Secondary (recrystallized or re-equilibrated melt inclusions), (2) Decrepitation clusters with saline aqueous fluid inclusions around the secondary inclusions and (3) Tertiary fluid inclusions (homogeneous, halite-saturated fluid inclusions).

The secondary re-equilibrated melt inclusions occur in the numerous aligned healed cracks within *titanite* (Fig. 14). These cracks are marked by numerous irregular-shaped dark inclusions (Fig. 14b) of different sizes. Within individual trails, there is only a slight variation in inclusion size. A second and probably recent crack system crosscuts these trails and is not healed, but is marked by alteration rims (Fig. 14b). The inclusions have an opaque appearance and a highly irregular shape irrespective of size (10–200 μm) with haloes and channels extending up to 50 μm into the titanite (Fig. 15), interpreted to represent re-equilibration and corrosion textures. The intensity of the re-equilibration texture is variable, even within a single trail. Only some smaller inclusions still exhibit negative crystal shapes (Fig. 16). Within these less re-equilibrated inclusions, a reddish entrapped mineral and a vapour bubble can be observed. The inclusions in *titanite* are too opaque for microthermometric measurements, but the presence of anhydrite, calcite and hematite was confirmed by Raman spectroscopy, despite the complexity of the titanite spectrum in the relative wavenumber range 200–1,600 cm^{-1}. These solid phases are similar to those observed in the primary inclusions in diopside. The interference of the

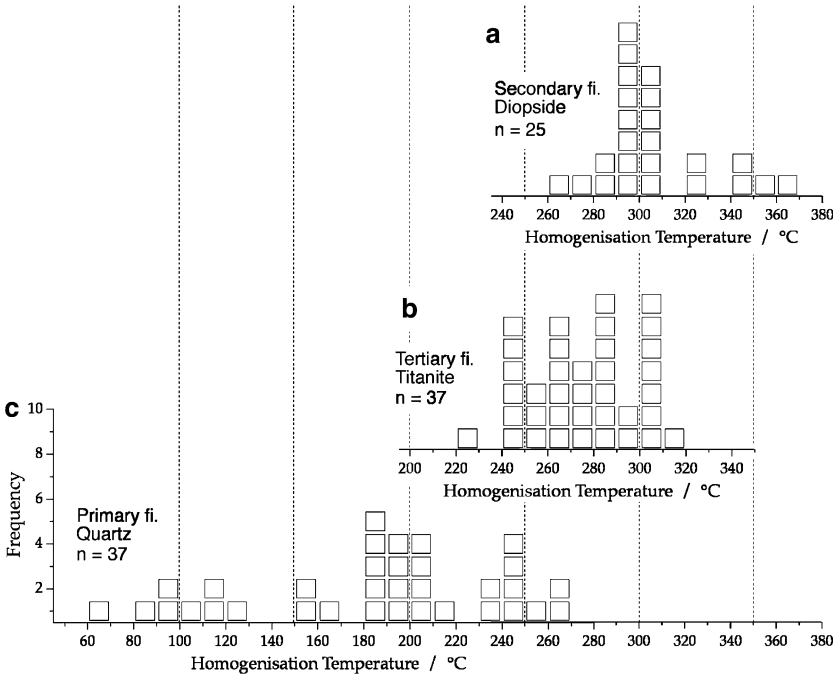

Fig. 13 Homogenization temperature histograms ($L + V \Rightarrow L$) of fluid inclusion in diopside (**a**), titanite (**b**) and pegmatitic quartz (**c**)

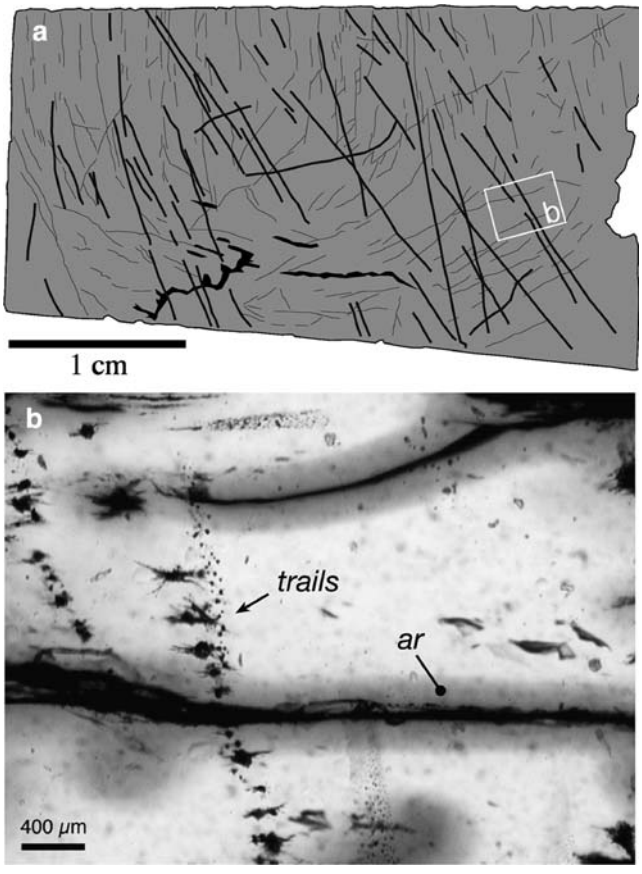

Fig. 14 **a** Schematic drawing of two sets of cracks (*thick* and *thin lines*) within a large crystal of titanite, of which only the *thick lines* are healed. **b** Microphotograph of healed fracture (*trails*) in the titanite (*thick lines* in **a**), and of open fracture (*ar*) with alteration rims (*thin lines* in **a**)

Raman signal of *titanite* and an aqueous solution in the range 2,900–3,700 cm^{-1} limits the interpretation of the water-spectrum, despite the confocal Raman setup. Careful subtraction of both spectra results in the identification of a highly saline aqueous solution within the fluid inclusion (see Appendix, Fig. 28). Anhydrite is also included as separate single crystal inclusions within these trails (Fig. 16c). Furthermore, anatase is detected in some inclusions (by Raman spectroscopy), which most probably is a retrograde alteration product of the *titanite*.

Both inclusions in decrepitation clusters (Fig. 17a) around the previously described secondary inclusions and inclusions in later healed cracks (Fig. 17b, c), that are different from those illustrated in Fig. 15b, contain similar fluids. These cracks were narrow and now contain flat inclusions with irregular shapes, but the walls are commonly defined by rational faces within the *titanite* crystal (Fig. 17b, c). These inclusions are indicated as *tertiary* inclusions. The phases present at room temperature in both types of inclusion associations comprise a homogeneous fluid (Fig. 9) containing a 7–10 vol.% vapour bubble and a 9–13 vol.% salt crystal, in addition to a highly saline fluid and sometimes a small hematite crystal; therefore, these tertiary inclusions in *titanite* are similar to the secondary fluid inclusions in diopside (cf. Fig. 12). Homogenization, i.e. $L + V \Rightarrow L$, occurs in a band between 240 and 310°C (Fig. 13b) without any pronounced highest frequency. These homogenization temperatures are slightly lower than those

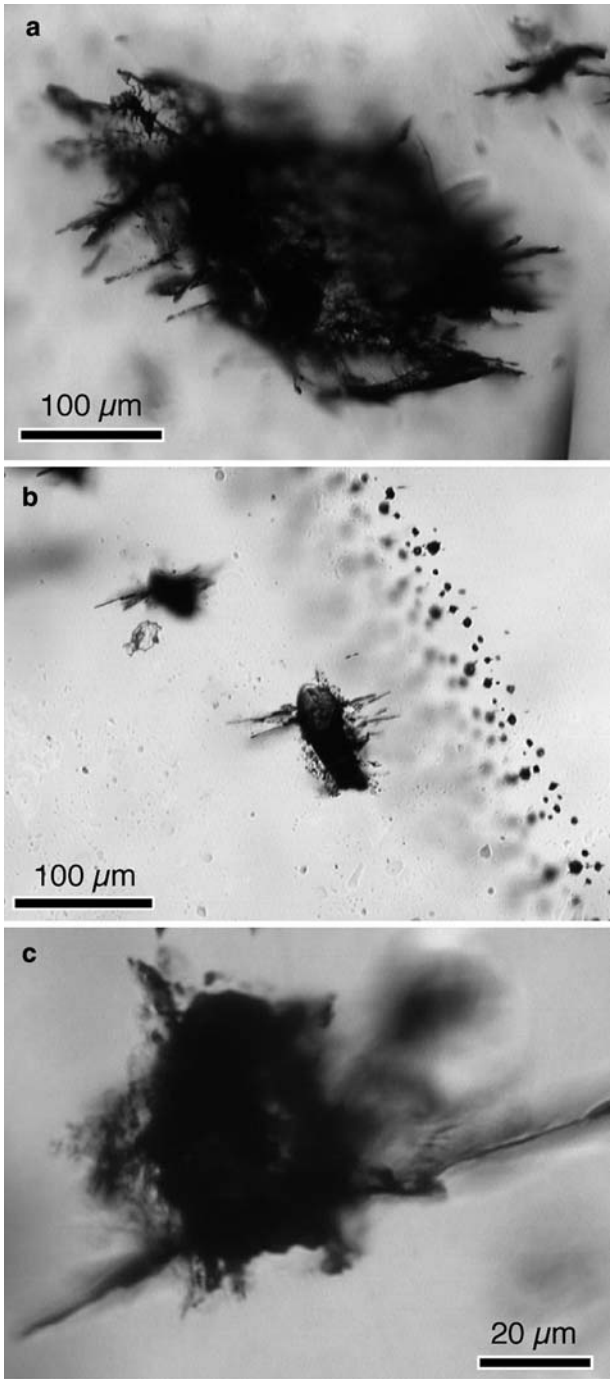

Fig. 15 Examples of different sizes of irregular-shaped dark inclusions in titanite, indicating intensive re-equilibration and corrosion

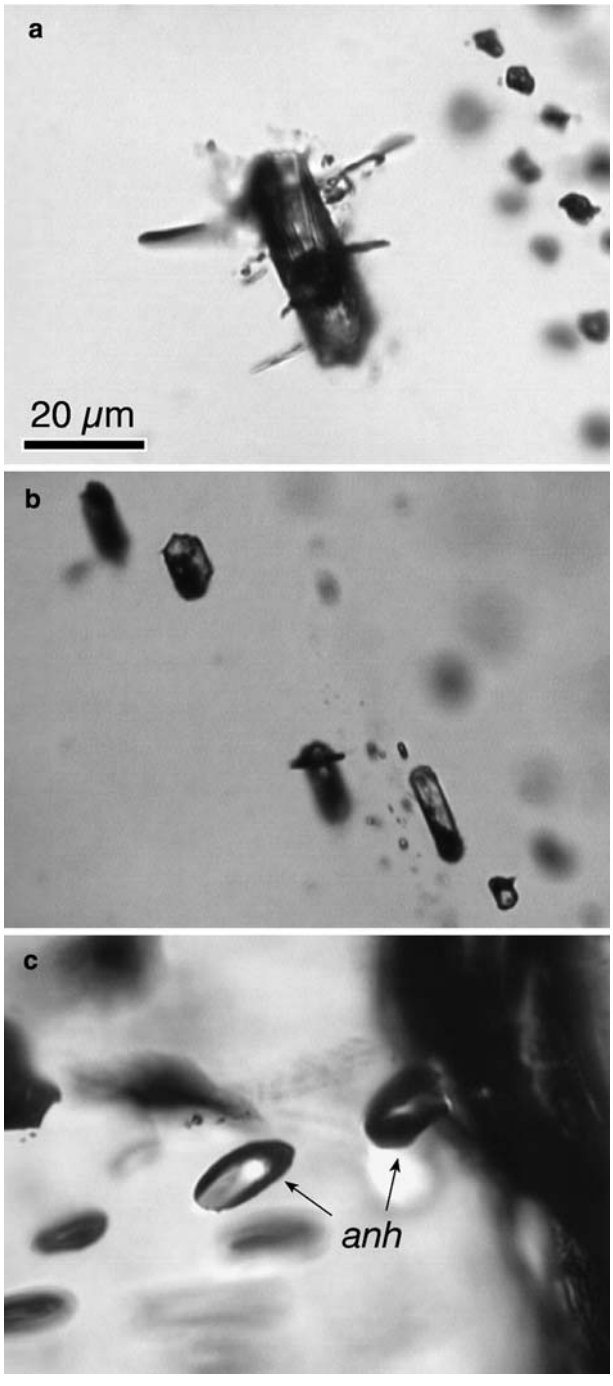

Fig. 16 Examples of nearly regular-shaped (*negative crystal*) inclusions in titanite, with minor traces of re-equilibration. *anh* anhydrite

measured in diopside (Fig. 13a). Dissolution of the halite crystals occurs in a narrow temperature range between 292 and 317°C (*tertiary fi-titanite* in Fig. 11), comparable to the temperature of halite dissolution in the diopside inclusions. Homogenization temperatures are both slightly higher and lower than dissolution temperatures, but they always occur in a relatively narrow temperature range. Calculated salinities vary between 35.3 and 39.9 eq. mass% NaCl, and molar volumes range from 22.4 to 22.8 cm^3 mol^{-1}, similar to the secondary fluid inclusions in diopside.

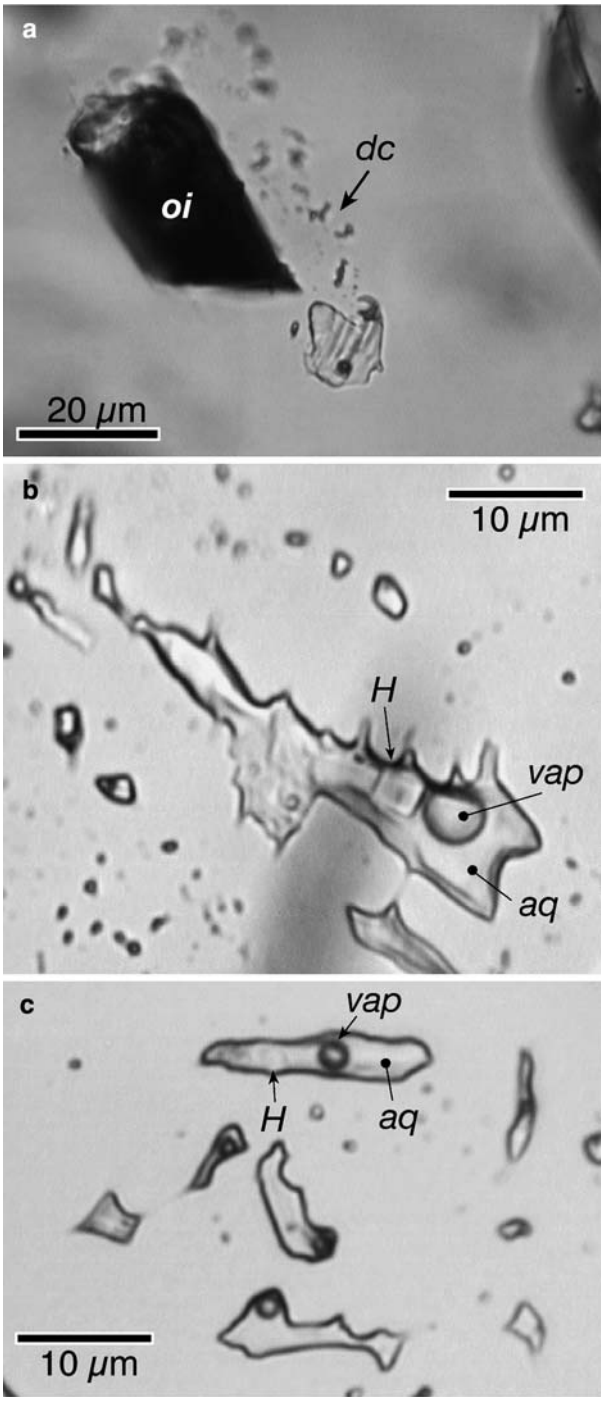

Fig. 17 **a** Example of re-equilibration textures around original inclusions (*oi*) with decrepitation clusters (*dc*) with fluid inclusions containing a vapour bubble, halite crystal and a highly saline aqueous solution. **b** and **c** Examples of healed fractures in titanite, with fluid inclusions containing a vapour bubble (*vap*), halite cube (*H*) and a highly saline aqueous solution (*aq*)

Quartz in diopside–titanite veins

Minor amounts of *quartz* associated with the diopside–titanite veins contain many fluid inclusions occurring both in trails and clouds, with a highly variable content. A compositional distinction is made between two types of fluid: (1) highly saline multiple phase, $V + L + S$ (Fig. 18), and (2) lower saline two phase, $V + L$ (Fig. 19). The distribution of the many inclusions does not allow a strict distinction between primary and secondary. Both assemblages are indicated as *primary fi quartz* in Figs. 11 and 13c.

Most fluid inclusions of the first type consist predominantly of a highly saline aqueous liquid solution, a halite cube and a vapour bubble, but their relative abundances in single assemblages are highly variable (Fig. 18a, b). The vapour bubble is absent in some inclusions, whereas others consist of euhedral halite crystals, attached to dark vapour bubbles (Fig. 18c). This illustrates that salt can be accidentally trapped and preserved in quartz in the absence of a fluid phase. Locally, a collection of several salt crystals and other entrapped minerals make up more than 90 vol.% of the inclusions (Fig. 18d), resembling primary inclusions in diopside (cf. Fig. 10c). A few hematite crystals are also included (Fig. 18e), again, in variable amounts. Similar to hematite in inclusions in diopside and titanite, it is an accidentally trapped mineral, which is also evidenced by hematite crystals exceeding the dimensions of the fluid inclusions.

The second type of fluid inclusions (Fig. 19) is of a lower salinity fluid with a highly variable filling degree. They may be completely filled by an aqueous liquid (Fig. 19a), or they may contain up to 90 vol.% vapour bubble (Fig. 19d). All-liquid inclusions, i.e. with 100 vol.% of aqueous solution, are more abundant. The variable relative sizes of vapour bubbles reflect heterogeneous trapping of liquid and vapour fluid phases.

The measured homogenization temperatures, i.e. $L + V \Rightarrow L$, and the melting temperatures of ice, hydrohalite and halite in the first type of fluid inclusions show large variations. Locally, a eutectic temperature of about –21.3°C was obtained, indicating the presence of a nearly pure NaCl–H_2O binary fluid system. The homogenization temperatures vary between 60 and 270°C (Fig. 13c), and are lower than those measured in titanite and diopside. The huge variation in salinity is reflected by the range in dissolution temperatures of halite (Fig. 11). A maximum dissolution temperature of 465°C was measured, whereas lower salinities are illustrated by the metastable melting of hydrohalite at +0.2°C. Calculated salinities vary between 26.3 and 55.2 eq. mass% NaCl and molar volumes range from 19.5 to 21.9 $cm^3\ mol^{-1}$, which significantly differ from the fluids found in inclusions in diopside and titanite. The *quartz* has grown under

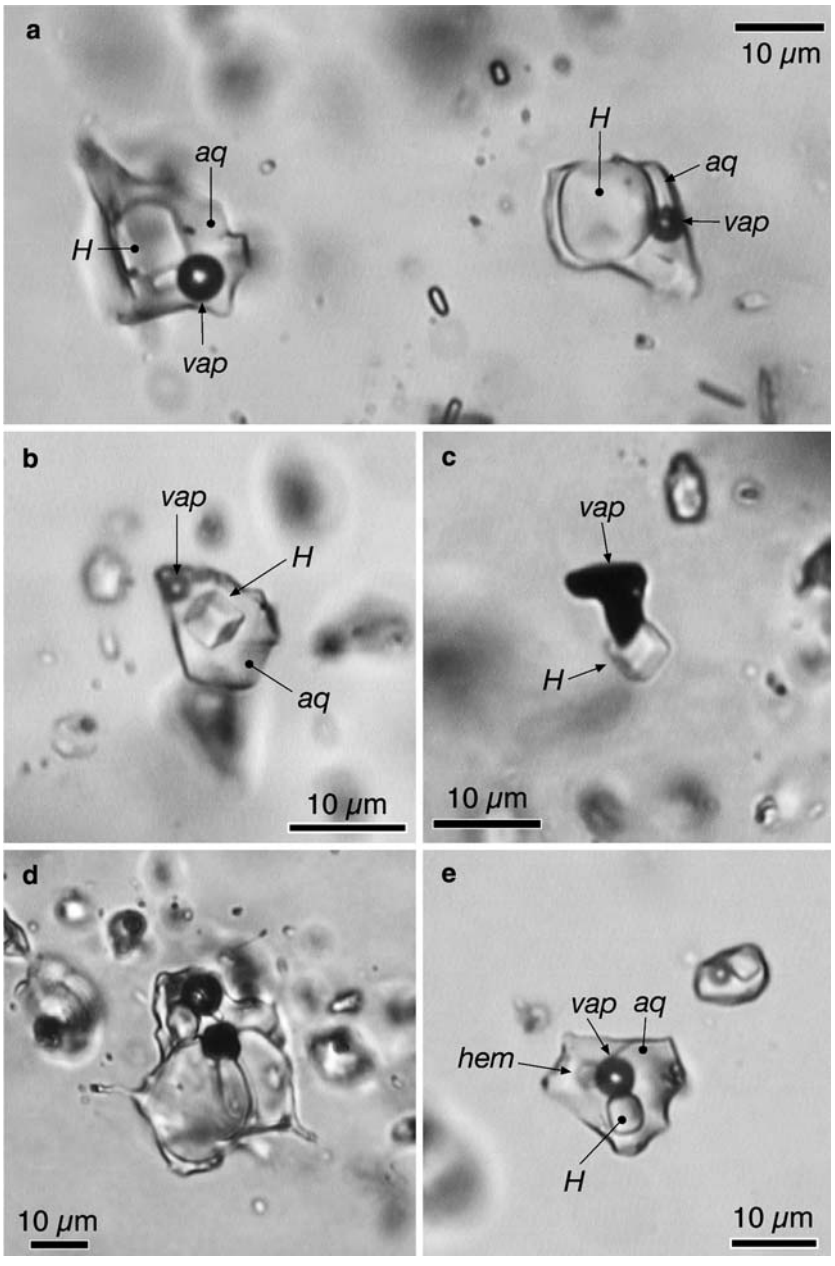

Fig. 18 Examples of the variety of fluid inclusions in the first stage of quartz (pegmatitic). Three phase (**a** and **b**)—vapour bubble (*vap*), halite cube (*H*) and aqueous solution (*aq*) with various proportions. Two phase—halite cube and vapour bubble (**c**). Multiple phase (**d**). Four phase (**e**)—vapour bubble, halite cube, hematite crystal (*hem*) and aqueous solution

highly variable fluid conditions, which only partly correspond to the secondary fluids found in diopside and titanite, and occasionally has more similarities with the primary inclusions found in diopside (Fig. 9).

Late-stage calcite, fluorite and quartz

The later stage mineral association of bladed *calcite*, *fluorite* and the second generation of *quartz* also contains abundant fluid inclusions, and is associated with the purely hydrothermal quartz–hematite mineralizations (Fig. 9). The *calcite* contains regularly shaped inclusions with negative crystal shapes (Fig. 20) up to 30 μm in diameter, either flat or equidimensional, or a combination of these shapes. They can be closely distributed, at only a few micrometres apart from each other. The inclusion assemblage contains a homogeneous fluid with about 8–10 vol.% vapour bubble and a nearly pure H_2O liquid. Nucleation of ice during freezing experiments caused disappearance of the vapour bubble, i.e. a complete collapse. Consequently, metastable melting of ice was measured up to +4°C. Stable melting of ice in the presence of a vapour bubble could only be measured in inclusions that partly

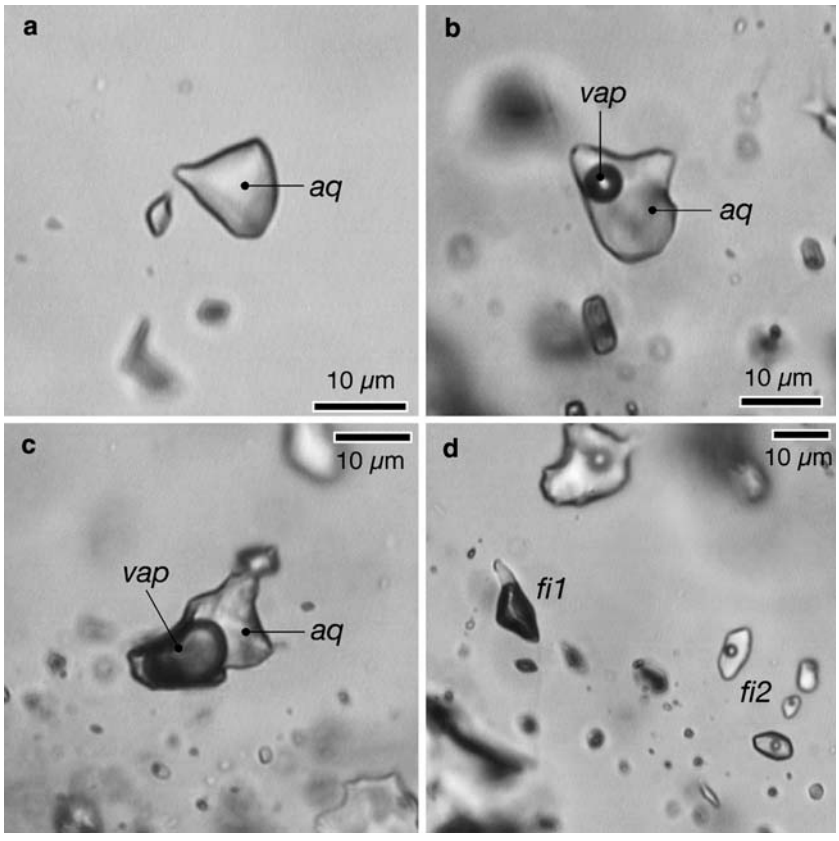

Fig. 19 Examples of heterogeneous two-phase inclusions ($L + V$) in the late-stage pegmatitic quartz containing variable amounts of vapour bubble and aqueous solution. *fi1* and *fi2* (in **c**) illustrate heterogeneous trapping

decrepitated during heating/freezing runs and illustrate the nearly pure H_2O character of the fluid (T_M around 0.0°C). Total homogenization, i.e. $L + V \Rightarrow L$, occurs in a range of 70–160°C, with a frequency mode at 130–140°C (Fig. 21a), corresponding to a calculated molar volume of 18.47–19.66 cm^3 mol^{-1}. The variation of T_H between distinct groups of inclusions within individual *calcite* grains is very small, but it indicates fast growth during distinct fluid pulses with slightly different properties through the system.

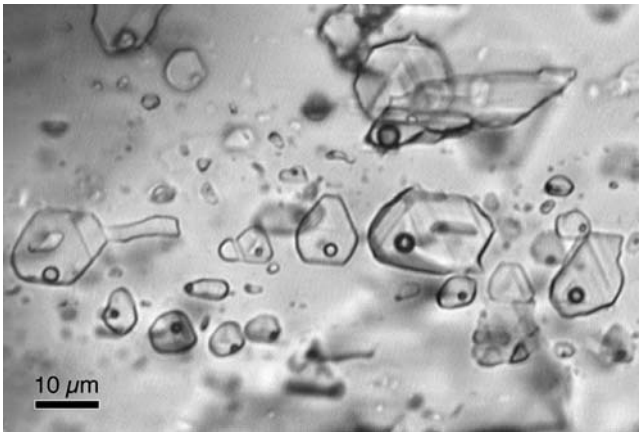

Fig. 20 Flat two-phase fluid inclusions ($L + V$) in bladed calcite, all with regular negative crystal shapes

Fluorite contains primary fluid inclusions with negative crystal shapes (tetrahedral), up to 20 μm in diameter (Fig. 22a, b), and trails of healed cracks with abundant secondary fluid inclusions (Fig. 22c) cut through both green and purple *fluorite*. Most of the primary inclusions contain a homogeneous fluid of pure H_2O with 8–10 vol.% vapour bubble. Total homogenization occurs in a range between 130 and 165°C into the liquid phase (Fig. 21b). Tetrahedral-shaped inclusions in the purple bands of *fluorite* contain variable amounts of H_2 (Raman detected, see Appendix, Fig. 29). The Raman peaks $\Delta\nu$ differ slightly from the values given by Dubessy et al. (1988), which is caused by a band-shift as a function of internal pressure, i.e. fluid density within the inclusions. Some inclusions contain a mixture of H_2O–H_2 (Fig. 22a) whereas others may contain pure H_2 (Fig. 22b), reflecting heterogeneous trapping. The secondary inclusions have irregular shapes and are of a homogeneous population with 7–9 vol.% vapour bubble. They contain only H_2O, similar to the primary inclusions in green *fluorite* and to those found in calcite (Fig. 20). Individual trails may have slightly different total

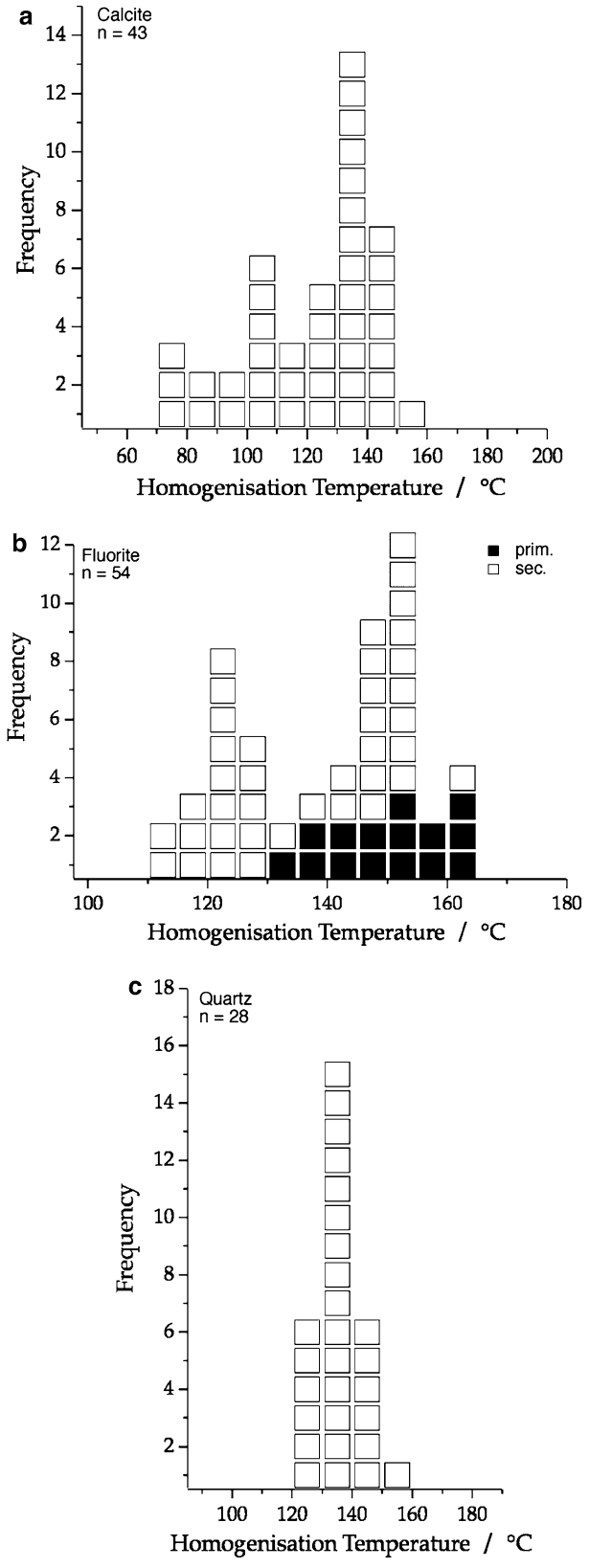

Fig. 21 Histograms with total homogenization temperatures ($L + V \Rightarrow L$) of fluid inclusions in calcite (**a**), fluorite (**b**) and late-stage quartz (**b**). *prim* primary fluid inclusions, *sec* secondary fluid inclusions

homogenization temperatures, e.g. in the range of 120–125 and 150–155°C (Fig. 21b), corresponding to molar volumes of 19.14 and 19.70 cm^3 mol^{-1}, respectively.

The Brazil twins in the late-stage *quartz* are partly marked by the variable occurrence of fluid inclusions (see Fig. 7). Most of the inclusions consist of a single phase, either liquid or vapour (Fig. 23a, b), and have an irregular shape, with sizes up to 20 μm in diameter. Distinct zones in single crystals are characterized by the presence of a homogeneous aqueous fluid, which may differ slightly in density from other zones. Locally, zones with two phase inclusions occur, containing a constant 8–12 vol.% vapour bubble (Fig. 23c). The inclusions are similar to those found in the bladed calcite (cf. Fig. 20). Stable melting of ice in the frozen inclusions occurs at about –0.4 to 0.0°C in the presence of a vapour bubble. In the absence of this bubble, metastable melting temperatures may be as high as +0.7°C. Total homogenization, i.e. $L + V \Rightarrow L$, of two-phase inclusions occurs at about 130–140°C (Fig. 21c), similar to the inclusions in calcite, and corresponding to a molar volume of 19.18–19.69 cm^3 mol^{-1}.

Interpretation of fluid and mineralization history

Pegmatitic origin of diopside–titanite veins

The origin of the diopside–titanite veins or dikes is either igneous, hydrothermal or a combination reflecting a transition from an igneous to a hydrothermal system (pegmatitic). In principle, pegmatites are relatively coarse-grained igneous rocks, with a highly variable grain size in which individual crystals reach several centimetres to several metres (e.g. Jahns 1955; Best 2003; London 2005). Grain size alone is, however, not diagnostic for a pegmatite, as hydrothermal or metasomatic systems may also develop exceedingly large crystals. Mineralogical and textural evidence may further constrain the igneous origin. Moreover, primary inclusions (fluid and melt) within the pegmatitic mineral assemblage are excellent indicators of either an igneous or a hydrothermal origin, as they are relicts of the environment of crystallization. These arguments can be directly used to identify the origin of the studied diopside–titanite veins. Their igneous origin may be deduced from: (1) the size of individual diopside and titanite crystals (up to 60 cm); (2) graphic intergrowth of diopside and albite associated with granitic pegmatites; (3) primary inclusions with a wide variety of compositions, ranging from highly saline aqueous fluids

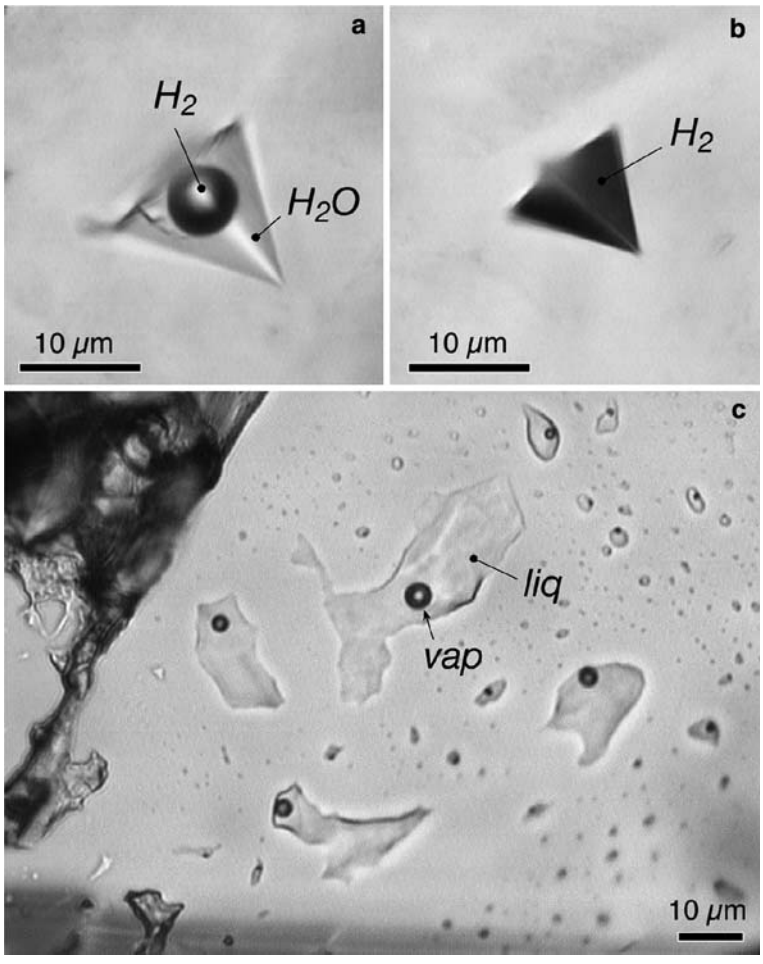

Fig. 22 Microphotograph of primary H_2–H_2O fluid inclusions in fluorite (**a** and **b**) with variable amounts of H_2-vapour bubble. **c** Secondary H_2O fluid inclusions

with high homogenization temperatures (exceeding 600°C) to recrystallized glassy inclusions with deformed vapour bubbles, i.e. relicts of a mixed silica–salt melt.

Some of those arguments can also be used, but only in part, for a hydrothermal origin of the studied veins. The graphic intergrowth may be regarded as a hydrothermal replacement feature. The K-feldspar phenocrysts in the granitic pegmatite at the contact with diopside–titanite veins are strongly albitized, which might be the result of a hydrothermal event (e.g. Nijland and Touret 2001). The timing of the replacive albite, however, is uncertain, and may not be cogenetic with the albite–diopside graphic intergrowth. The presence of primary highly saline aqueous inclusions is a direct indication of a hydrothermal origin, which may be derived from a magmatic fluid. Coexisting recrystallized melt inclusions illustrate that the diopside may have formed at the interface of an igneous and hydrothermal system at high temperatures, i.e. immiscible saline fluid (volatiles) and silicate melt (see also Shmulovich et al. 1995), typical for a pegmatitic system.

The composition of the diopside–titanite dikes classifies them as mafic pegmatites. This class of pegmatites includes nelsonites, i.e. Fe–Ti oxide pegmatites (e.g. Lister 1966; Scoon and Mitchel 1994; Florence et al. 1995; Cox et al. 1998), and olivine–clinopyroxene pegmatites (e.g. Viljoen and Scoon 1985; Scoon and Mitchel 1994). In these studies, grain size has been the main criterion to classify these rocks as pegmatites. In general, pegmatites are associated with a large mass of plutonic rock, usually granites (e.g. Best 2003). Mafic pegmatites are associated with anorthosite complexes, and can have a replacive origin (e.g. Scoon and Mitchel 1994). The studied diopside–titanite dikes do not have any chemical affinities with nearby exposed granitoid bodies (e.g. Mt Neill Porphyry, British Empire Granite, see Fig. 1).

As previously mentioned, the diopside–titanite veins have only partial compositional affinities with agpaitic and miaskitic nepheline syenites (cf. Wallace

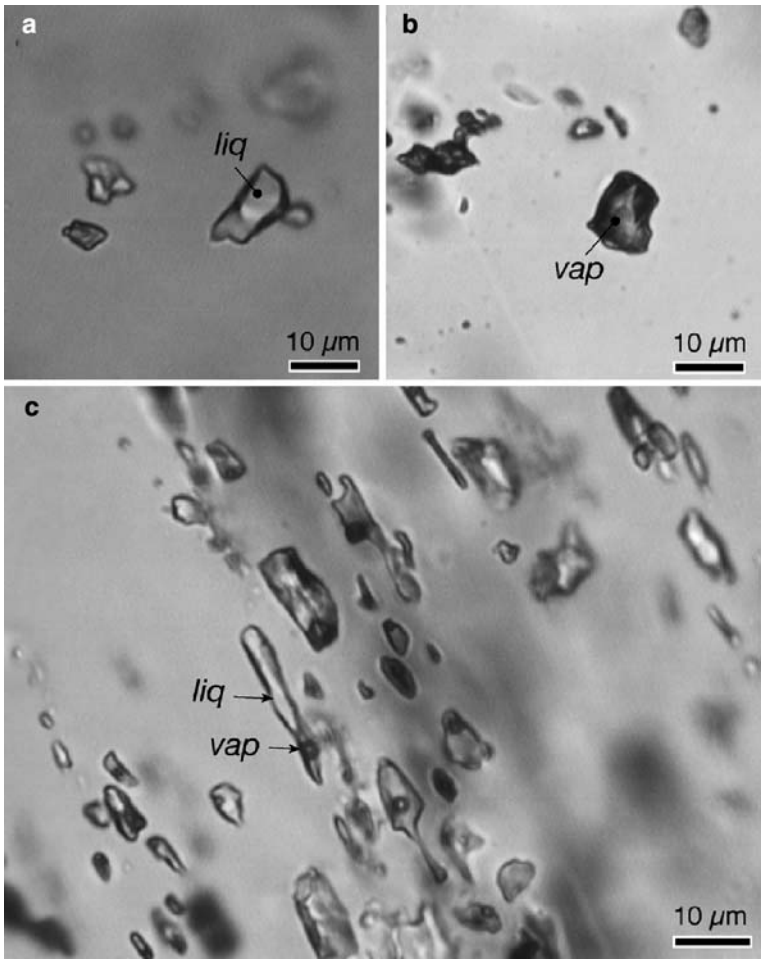

Fig. 23 Examples of fluid inclusions in latest quartz mineralizations—all liquid (**a**), all vapour (**b**) and two-phase inclusions (**c**)

et al. 1990; Arzamaststev et al. 2000), although the presence of massive diopside–titanite veins is never revealed in those studies. These rocks may occur in dykes and crosscut major intrusive syenite complexes. Pyroxenite enclaves or bands can also be associated with syenitic rocks (e.g. Dorais 1993; Ferreira et al. 1994), representing liquid immiscibility within the magma chamber. Calcic pyroxene-bearing granitic pegmatites may be associated with amphibole syenites in composite alkalic intrusives (e.g. Falster et al. 2000). The diopside–titanite dikes in our study may, therefore, represent the fractionated melt from a calcium-rich syenitic system, which is not exposed in the Mt Painter Inlier. They could also be dismembered parts of an unexposed anorthosite complex, from which aluminium had been removed by anorthite fractionation. Troctolite and gabbro found in Hidden Valley (''Alteration zone'' in Fig. 1), located 20 km to the northeast within the Mt Painter Inlier, may also belong to this suite of mafic intrusives.

Titanite

Titanite-bearing assemblages can be used as an indicator of T-P-$x(CO_2)$ conditions at various grades of metamorphism (Hunt and Kerrick 1977). The thermodynamic stability (equilibrium conditions) of a titanite is defined by the presence of a CO_2-rich fluid, which is, however, absent in the studied diopside–titanite veins. The breakdown of a diopside–titanite assemblage can occur according to the reaction: 5 diopside + titanite + 4 CO_2 + H_2O = tremolite + rutile + 3 quartz + 4 calcite. Both rutile and tremolite have not been observed in the veins. Titanite is probably not involved in the late-stage massive alteration of diopside into actinolite. In complex natural systems, however, the number of components (in both fluid and solid phases), the oxygen fugacity in the rock and the presence of quartz (e.g. Spear 1981) will influence the titanite stability. Thermodynamic modelling by Xirouchakis et al. (2001a, b) illustrates that a system containing both diopsidic pyroxene and titanite is not tightly constrained by temperature, pressure and

oxygen fugacity. However, the fluids calculated by Xirouchakis do not correspond to any type of the observed fluids in inclusions in the present study.

Titanite in veins, dikes, syenitic or granitic host rocks usually occurs as an accessory mineral, and does not exceed grainsizes of a few millimetre (e.g. Gieré and Williams 1992; Pan et al. 1993; Della Ventura and Bellatreccia 1999), which is in sharp contrast to the observed single crystals up to 40 cm in this study (see Fig. 2). Titanite may have accommodated REEs and Y in variable amounts, which can be coupled to a substitution of Ca and Ti (Zabavnikova 1957). Titanite in our studied veins shows a negative correlation between (Ca, Ti) and (REE, Y, Al, Fe^{3+}) content (Fig. 24). The shift of data points below the 1:1 line (i.e. the previously mentioned substitution), however, indicates incomplete element exchange, or the lack of other REE electron microprobe analyses. The calculated oxygen content of nearly 20 based on 4 Si (see Table 2) indicates the presence of only small amounts of other anions, like (OH, F), which is also confirmed with Raman spectroscopy (see Appendix, Fig. 28). Similar titanite compositions, i.e. rich in REEs and Y, have been found in fine-grained alkali syenites (e.g. Della Ventura and Bellatreccia 1999), granites and granitic pegmatites (e.g. Pan et al. 1993); these authors suggest similar substitution mechanisms. Relatively high concentrations of LREEs indicate a high degree of fractionation of the parent melt during crustal emplacement or an originally enriched melt source.

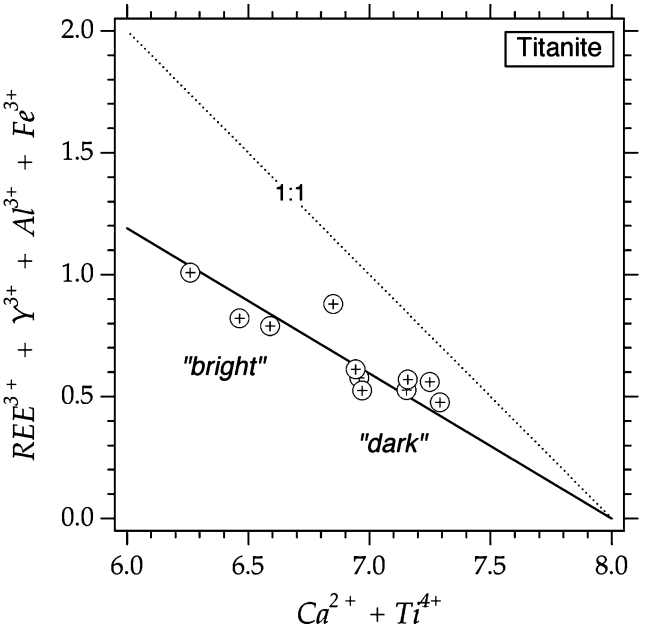

Fig. 24 Compositional variation within titanite. The 1:1 line has a slope of –1.0 and represents stoichiometric substitution. *Bright* and *dark* correspond to the zonation described in Tables 1 and 2

Similar enrichments are observed in nelsonites (e.g. Cox et al. 1998), where LREEs are mainly present in apatite.

Based on evidence from fluid and melt inclusions, titanite is considered to have crystallized before diopside (Fig. 9). The complex heterogeneous inclusion assemblage found in healed cracks in titanite (''secondary'') is similar to that found in ''primary'' inclusions in diopside. The titanite does not contain any type of primary inclusions. Slight cooling or deformation of the titanite crystals in this early stage resulted in the formation of cracks. These cracks healed, trapping the highly saline fluid that exsolved from the residual melt during the ensuing crystallization of the diopside in the remaining space within the open veins. The fluid part of this heterogeneous mixture of rest-melt and highly saline aqueous fluid is characterized by the presence of already-crystallized minor amounts of calcite, anhydrite and magnetite, and mainly consists of abundant salt crystals and a saline-saturated aqueous solution. This heterogeneous fluid and rest-melt is trapped in different proportions within both diopside and titanite, causing a large variation in inclusion appearances. The rest-melt from which first titanite and then diopside were formed must have been rich in elements like Ca, Ti, Mg, Si with moderate amounts of Fe, whereas Al, Na and K were absent or stabilized within the melt due to complexing. This melt also contained minor amounts of Cl, F, Y, LREE and H_2O, of which especially Y, LREE and H_2O are included within the titanite.

Titanite in the veins has previously been dated by U–Pb at 443 ± 2 Ma (Elburg et al. 2003). Although the natural leaching processes of titanite may cause the mobility of REE, U and Th (Pan et al. 1993), the measured U–Pb age is close to being concordant, suggesting that leaching did not affect the titanite that was dated, or that leaching took place very shortly after titanite formation. The post-Delamerian age is supported by the absence of ductile deformation in the veins. This age is indistinguishable from the U–Pb monazite age of the I-type phase of the British Empire Granite at 441 ± 1 Ma (Elburg et al. 2003). This is a mixed I–S type granitic batholith with an exposed area of 30 km^2, located at the core of the Mount Painter Inlier, and of which the centre is located 20 km to the northeast of the vein location. The granite probably continues at depth, since the Mt Painter Inlier is characterized by a pronounced gravity low (S. Hore, personal communication). It is therefore likely that the diopside–titanite veins are a manifestation of the same magmatic pulse as the one to which the British Empire Granite belongs. It is, however, hard to see a genetic

relationship between these granites, with MgO < 1%, CaO < 2% and TiO_2 < 0.4%, and the veins, which are characterized by extreme enrichments in these elements. Since Nd isotopic data point towards a mantle component in the I-type phase of the British Empire Granite (Elburg et al. 2003), more mafic rocks types could be present below the level of exposure, although the gravity data indicates that they cannot be very extensive. Nd isotopes indicate that the REE contents of the titanite are largely derived from the Mesoproterozoic granitic host rock (Elburg et al. 2003), but this cannot be the source for the major elements in the veins, since this granite is equally depleted in CaO, MgO and TiO_2 as the British Empire Granite (Neumann 2001).

Formation conditions of diopside–titanite veins

The primary inclusions in diopside suggest crystallization from a heterogeneous melt and fluid system, which is a common phenomenon in the formation of igneous rocks (e.g. Roedder 1984, chapter 14). It should be noted that fluid immiscibility occurs in addition to fluid/melt immiscibility. Most residual magmas (either shallow or deep) crystallize at conditions of the immiscibility in three phases (e.g. Shmulovich et al. 1995), i.e. a silicate melt, a highly saline aqueous solution (liquid-like) and a lesser saline gas (vapour-like) or floating salt crystals. This multiple immiscibility explains the huge variation in saline fluid inclusion properties that generally occur in association with intrusive rocks (e.g. Weisbrod 1981).

The presence of salt crystals, the compositional variation and high salinity values in primary inclusions in diopside measured in this study suggest formation conditions according to a fluid setting below the halite liquidus. In addition, microthermometrical results indicate formation conditions exceeding 600°C. Isochores of homogeneous primary fluid/melt inclusions in diopside cannot be calculated because equations of state for these chemically complex systems are not available. Homogenization of part of the inclusions, in this case dissolution temperatures of halite in aqueous solutions, can be used to trace isochores within a limited temperature range where the mutual solubility of saline fluid and melt is low (cf. with CO_2 homogenizations in a CO_2–H_2O fluid system). A hypothetical fluid composition of 80 mass% NaCl is chosen to illustrate possible trapping conditions of primary inclusions in diopside and secondary inclusions in titanite (Fig. 25a). This composition does not represent the true salinity of the system but lies within the range of measured salinities. A fluid of 80 mass% NaCl is heterogeneous below approximately 260 MPa along the calculated isochores (Fig. 25a). The observed inclusion assemblage clearly reveals fluid heterogeneity;

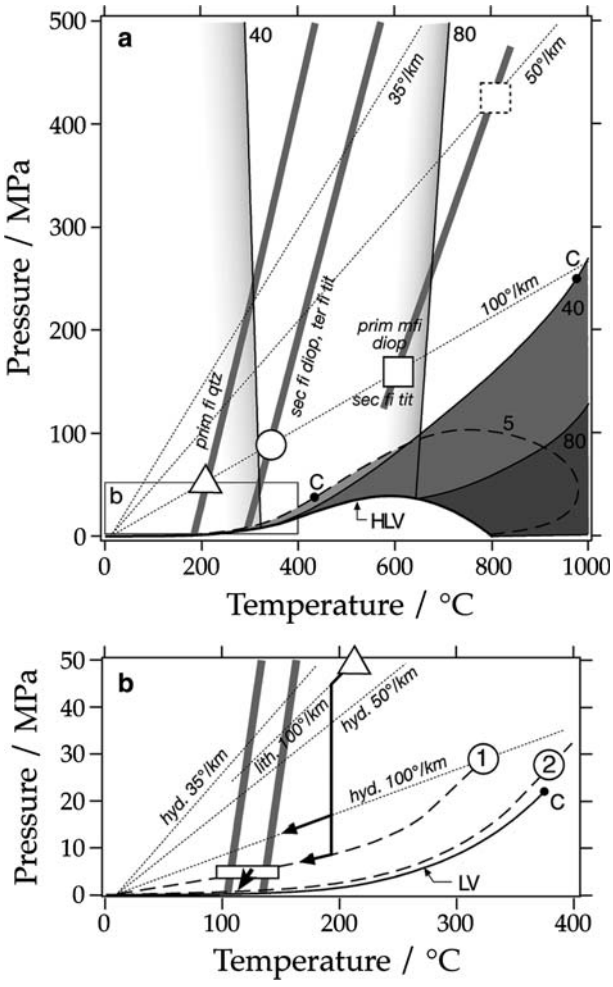

Fig. 25 **a** Temperature–pressure diagram with possible formation conditions of the pegmatitic system. Phase equilibrium in the H_2O–NaCl system are calculated with Anderko and Pitzer (1993) The *shaded areas* indicate *LV* immiscibility—80, 40 and 5 correspond to 80, 40 and 5 mass% NaCl, respectively. *HLV* equilibrium line of halite, vapour and liquid, *C* critical points of 5 and 40 mass% NaCl solutions. The nearly *vertical solid lines* indicated the liquidus of 40 and 80 mass% NaCl solutions. The *short dashed lines* are lithostatic geothermal gradients for 35, 50 and 100°km^{-1}. Isochores are illustrated with *thick grey lines*. The *square*, *circle* and *triangle* illustrate formation conditions of inclusions in diopside, titanite and quartz. See text for further details. **b** Temperature–pressure diagram with three hydrostatic geothermal gradients (hyd. 35 km^{-1}, hyd. 50 km^{-1}, hyd. 100°km^{-1}) and one lithostatic geothermal gradient (lith. 100°km^{-1}). The *triangle* corresponds to the quartz formation conditions of the late pegmatitic stage (see also Fig. 28). The *arrows* (*T*) indicate the transition from a lithostatic to a hydrostatic fluid system. The *curved solid line* is the boiling curve (*LV*) of pure H_2O (*C* critical point). The numbers *1* and *2* illustrate typical geothermal gradients in geothermal systems. Isochores are indicated with *thick grey lines*. The *box* reflects formation conditions of the bladed calcite. The *short arrow* indicates pressure releases during growth of the second quartz generation

consequently, the formation conditions must correspond to a high geothermal gradient, e.g. the 100°km^{-1} in Fig. 25a. A homogeneous highly saline fluid can only be trapped at higher pressures along the isochores, which correspond to lower gradients (see dashed box in Fig. 25a). We do not know the depth at which the diopside–titanite dikes formed, but high gradients can be expected for igneous bodies. Trapping conditions around 510 ± 20°C and 130 ± 10 MPa for a fluid of 61 mass% NaCl probably represent minimum formation conditions, as inclusions are observed with higher salinities (locally halite melting temperatures exceed 600°C).

Transition to a pure hydrothermal system in a late pegmatitic stage

The salinity of the fluid in this study, as previously mentioned, is suggested to be obtained from a magmatic source and represents an exsolved fluid. The secondary fluid inclusions found in diopside (Fig. 12) and the tertiary inclusions found in titanite (Fig. 17) are formed from a homogeneous fluid, as shown by the homogeneity of the inclusion population (Fig. 11). After formation of the diopside and titanite in a pegmatitic system, this remaining fluid has a lower salinity of approximately 40 mass% NaCl. Two mechanisms may lower the bulk salinity of pore fluids: (1) preferential removal of halite crystals as the fluid system becomes saturated and (2) addition of an external aqueous meteoric fluid. Both mechanisms of reducing the salinity are suggested to be active in our studied samples. Reducing the salinity of a fluid at constant temperature and pressure can move the system into the field of homogeneous fluid conditions (see Fig. 25a). Campbell et al. (1995) report a similar trend in inclusions in quartz veins, which formed from magmatic fluids in a granitic complex. They could not assign the origin of the bulk salinity unambiguously to either a magmatic source, as suggested by isotopic data, or an evaporitic source, reflected by halogen ratios.

The rock system contains a homogeneous fluid above 300°C and above 50 MPa (Fig. 25a) along calculated isochores of secondary inclusions in diopside and tertiary inclusions in titanite. Intersection of the calculated isochores with the previously selected hypothetical 100°km^{-1} gradient confirms formation conditions within the homogeneous fluid field at about 350 ± 20°C and 80 ± 10 MPa. However, this high gradient is unlikely to have remained the same if it was induced by magmatic activity, and higher pressures are more likely to be obtained from lower gradients. This homogeneous fluid must have contained minor amounts of small hematite flakes, floating freely around, which consequently are trapped accidentally in a few inclusions. This hematite is probably an oxidation product of the previously mineralized magnetite in the early pegmatitic stage.

Further cooling of the rock system causes the fluid system to cross the liquidus of the 40 mass% NaCl fluid system (Fig. 25a). Consequently, halite precipitates again as small crystals in major amounts and causes the heterogeneity of the fluid. Simultaneously, this fluid becomes saturated with silica and quartz mineralizes (Fig. 9). The associated fluid inclusion assemblage found in this late pegmatitic stage quartz illustrates this highly variable salinity and bulk density (Figs. 11 and 14), conforming to these heterogeneous formation conditions around 200 ± 20°C and 50 ± 10 MPa along the hypothetical 100°km^{-1} gradient. The relatively high homogenization temperatures result from the entrapment of mechanical mixtures of individual phases in the heterogeneous fluid system. The accidentally trapped halite in quartz (Fig. 18c) illustrates that salt crystals were present and can be preferentially separated from the fluid. Hematite is still present in minor amounts in this fluid and is accidentally trapped in a few inclusions (Fig. 18e). Further lowering of the bulk salinity of this fluid is most probably caused by dilution with infiltrating meteoric fluids.

Re-equilibration of inclusions in titanite

Re-equilibration (or corrosion) of secondary inclusions in titanite occurred after crystallization of the diopside during the transition to a purely hydrothermal system. A textural comparison with re-equilibrated fluid inclusions in natural quartz (e.g. Ayllon et al. 2003) and with experimental studies (e.g. Sterner and Bodnar 1989) indicates the similarity with underpressurized fluid inclusions. These studies describe the development of irregular textures with a number of re-entrants and small inclusion-free microfractures around parent inclusions that tend to close. The irregularity turns the parent inclusions into dark features in which separate phases are hardly recognizable, similar to the inclusions found in the studied titanite (see Fig. 15). Furthermore, decrepitation clusters were developed in experimental studies, similar to the features observed in our titanite samples (see Fig. 17). These arguments strongly suggest that the re-equilibration of the highly saline inclusions in titanite was caused by an internal underpressure that developed during cooling.

The homogeneous fluid found in the inclusions in the subsequently healed decrepitation clusters indicates that the re-equilibration process took place at similar conditions under which the secondary fluid inclusions were trapped in diopside. Re-equilibration textures are absent in diopside, due to the relative weakness of the crystals along its cleavage planes. Any pressure differences between the surroundings and the inclusions would immediately destroy the original inclusions by rupture. Furthermore, the retrograde alteration of diopside to actinolite erased many of the original textures.

Mobility of light rare earth elements and yttrium

Original magmatic REEs can be remobilized by hydrothermal and metasomatic processes (e.g. Oliver et al. 1999; Wang and Williams 2001). Magmatic fluids may contain relatively high concentrations of LREEs, as illustrated by crush-leach analyses from inclusions in quartz (e.g. Banks et al. 1994) and daughter crystals (e.g. Kwak and Abeysinghe 1987). Mobilization of LREEs from titanite (see also Pan et al. 1993) is evident from the precipitation of allanite, apatite and wakefieldite in a subsequent mineralization phase (Fig. 9). The observed irregular zonation in titanite (Fig. 5) is of secondary origin, reflecting the leaching processes of LREEs and yttrium. Yttrium must have been preferentially partitioned in the fluid phase, as it only reappears in minor amounts in subsequent mineralizations. In addition, manganese has also been mobilized as evidenced from cogenetic Mn-rich actinolite (Tables 3, 4). Mn-actinolite, epidote/allanite, apatite and wakefieldite are not included within the first quartz phase and, therefore, must have formed below 200°C and 50 MPa, during further cooling (Fig. 25a). These conditions are more likely to belong to a hydrothermal event than to a magmatic event. Smith et al. (2000) report fluid inclusions in apatite and bastnäsite (a REE-rich carbonate) crystals formed at relatively low temperatures and pressures from dilute aqueous fluids in a multistage hydrothermal setting, unrelated to pegmatites. Similar formation conditions are deduced in this study (Fig. 25a), although fluid inclusions are absent in apatite and wakefieldite.

Quartz–hematite mineralizations, a palaeo-geothermal system

The previously described temperature–pressure development of the diopside–titanite veins is illustrated along a lithostatic geothermal gradient of $100°km^{-1}$ in Fig. 25a, including the transition from magmatic conditions (>600°C) to hydrothermal conditions around 200°C. This episode was followed by brecciation and a new purely hydrothermal event that partly fragmented the diopside–titanite veins and host rock (see Figs. 3, 4). A new fluid system was imposed on the rock that caused the alteration of diopside (Fig. 4b), magnetite and parts of the host rock. Major amounts of hematite precipitated. The fluid involved in this hydrothermal event is preserved in bladed calcite (Fig. 20), fluorite (Fig. 22) and the second quartz generation (Fig. 23), and consists of nearly pure water. These kinds of mineralizations have been described in several active geothermal systems (e.g. Simmons and Christenson 1994; Moore et al. 2000) and are regarded typical for a boiling fluid system. Therefore, the studied veins are likely to represent a palaeo-geothermal system. The platy habit of the calcite and the abundant occurrence of fluid inclusions are assumed to indicate a similar origin. The minor amount of mineralized calcite in the system indicates that it was still poor in CO_2, which again could not be detected by either Raman spectroscopy or microthermometry in the studied fluid inclusions. The fluid found in calcite is homogeneous within distinct inclusion populations, but differs slightly between populations, as illustrated by a variable T_H between 130 and 140°C (Fig. 21). It must be noted that a homogeneous fluid inclusion assemblage per definition represents formation under non-boiling circumstances, but the estimated formation conditions are near to boiling (Fig. 25b). In a geothermal system, $100°km^{-1}$ has been suggested as a typical average hydrostatic geothermal gradient (e.g. Ruggieri et al. 1999). However, temperature profiles in boreholes indicate a strongly variable and decreasing gradient, nearly parallel to the boiling curve of pure H_2O, at slightly higher pressures (see Fig. 25b). According to these gradients, trapping of primary fluid inclusions in calcite must have occurred at slightly higher pressures than in a boiling system, and varied between 1 and 5 MPa at temperatures between 100 and 140°C. Individual fluid inclusion trails in fluorite register individual pulses of hot fluids circulating in the system, and correspond to the measurements in the bladed calcite.

The formation of massive quartz mineralization is also typically for geothermally active systems (e.g. Moore et al. 2000). Coarsely grown quartz crystals are often zoned and associated with amorphous silica in this environment. The zonation in this study is mainly associated with Brazil twinning. The fluids found in the inclusions are similar to those in calcite and fluorite; therefore, similar formation conditions are valid for this quartz phase. However, quartz reveals some evidence

of real boiling, which can only be reached by sudden pressure releases above 100°C (Fig. 25b), possibly caused by sudden fluid release at the surface (geysers). Below 100°C, the vapour pressure of H_2O is lower than atmospheric pressure, and H_2O will remain in the liquid-like phase. Alternatively, occasional injections of gases like CO_2 may also cause this system to boil, as the vapour pressure of the fluid will increase, but no evidence is found for the presence of these gases.

Although diopside–titanite veins have only been found in a few locations, quartz–hematite veins and especially actinolitization are extremely common in the cover rocks around the Mt Painter basement. The extent of the fluid system must therefore have been considerable. The cause of this magmatic-hydrothermal event is yet unclear. The fact that there is a mantle signature within the Nd isotopes of the British Empire Granite (Elburg et al. 2003) precludes that the system has been driven by radiogenic heat production from the Mesoproterozoic A-type granites only. The idea that this mantle melting may be a far-field effect from subduction in the contemporaneous Lachlan Fold Belt to the east, or the orogenic event in the Harts Range to the north, needs further testing.

Hydrogen in fluorite and relationship to uranium mineralization

The origin of hydrogen fluid inclusions in fluorite is suggested to be radiolysis of H_2O caused by uranium-rich minerals (cf. Dubessy et al. 1988). The hydrogen occurs preferentially within the purple fluorite, which also includes some uranium mineralizations (radiation damage centres). These mineralizations are also proposed to be responsible for defining the colour of fluorite from green to purple that grew contemporaneously with the late hydrothermal quartz–hematite mineralization. Radiolysis of H_2O produces oxygen as well as hydrogen; however, O_2 has not been detected within these fluid inclusions. Differential escape of H_2 and O_2 from the fluid system may have caused different gas ratios among fluid inclusions (see also Dubessy et al. 1988).

Timing of events

We propose that the British Empire Granite, the diopside–titanite veins, the uranium mineralization and the quartz–hematite mineralization all belong to a single magmatic-epithermal event, which started at magmatic temperatures, and cooled down over time. Although we know when the event started (around 442 Ma), no good age constraints exist on the late epithermal quartz–hematite association, although U–Pb monazite dating implies an imprecise age of 440 ± 50 Ma (Elburg et al. 2003). We think that the epithermal event belongs to the same system as the magmatic one, and that therefore little time elapsed between the two. This is indicated by our inclusion studies, where hematite, typical for the late epithermal event, already starts appearing in the high-temperature secondary inclusions within the diopside. Our study shows that magmatic reworking of an area pre-enriched in, for instance, uranium in the form of A-type granites is an efficient way to form ore deposits. It also shows that the hydrothermal system, although strongly reminiscent of the 1,590 Ma Olympic Dam magnetite–hematite–REE mineralization, is driven by Palaeozoic rather than Mesoproterozoic magmatism. This may have implications for the economic prospectivity of the Mt Painter area.

Acknowledgments Marlina Elburg acknowledges an ARC Australian Post-doctoral Fellowship and an EU Marie Curie Fellowship. The Sprigg family is thanked for providing access to the veins on their property. Paul Bons, John Foden, Steve Hore, Justin Freytag, Ilka Hamann and Susanne Skora were of assistance during various stages of the research. Nick Oliver, Claire Ramboz, Jacques Touret and Bruce Yardley are thanked for reviewing this manuscript. Helmut Mühlhans is thanked for his assistance on the microprobe, and Johann Seiser for the preparation of thick-sections.

Appendix

Raman spectra of unusual mineral and fluid phases associated with the diopside–titanite veins

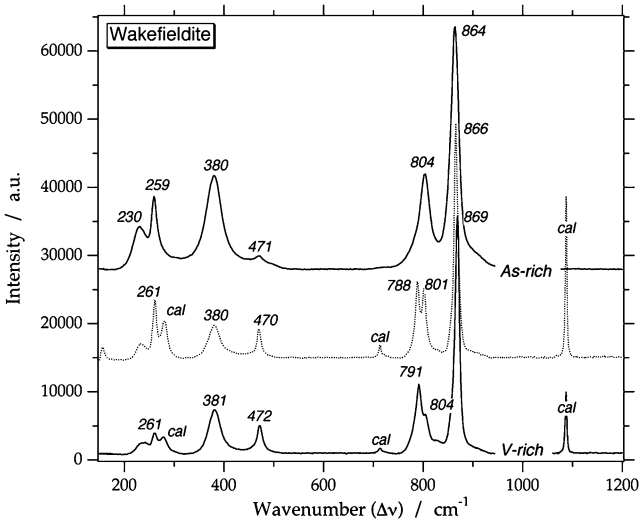

Fig. 26 Raman spectra of wakefieldite. The main peak of V-rich wakefieldite is positioned at about 869 cm^{-1}, whereas the As-rich wakefieldite has its main Raman peak at significantly lower wavenumbers, at 864 cm^{-1}

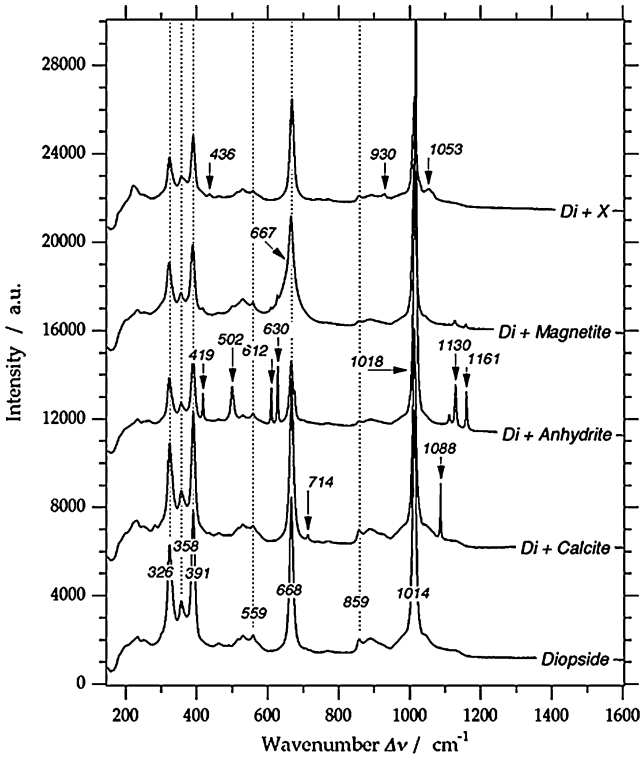

Fig. 27 Raman spectra of several solid phases in primary inclusions in diopside, including magnetite, anhydrite, calcite and an unknown mineral. The Raman signal is relatively weak compared to diopside due to the small size (< 5 μm) of entrapped minerals

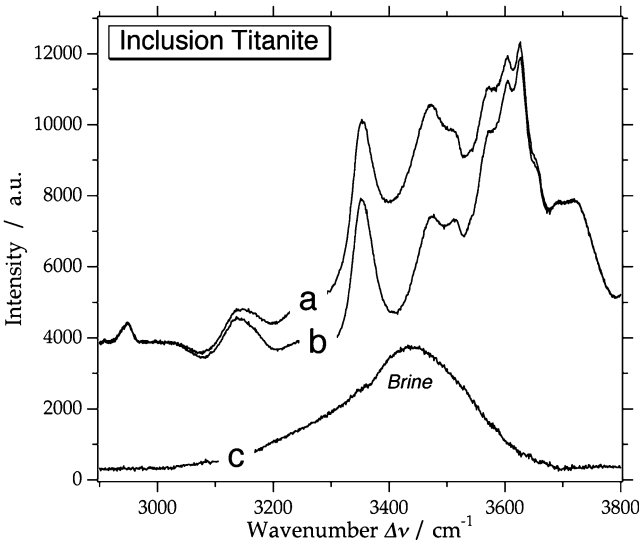

Fig. 28 Raman spectra of a secondary fluid inclusion in titanite (**a**) and pure titanite (**b**). The interference of the Raman signal of titanite and an aqueous solution in the range of 2,900 to 3,700 cm^{-1} limits the interpretation of the water spectrum. Careful subtraction of the spectra (**a** and **b**) result in the identification of a highly saline aqueous solution within the fluid inclusion (**c**), cf. Bakker (2004)

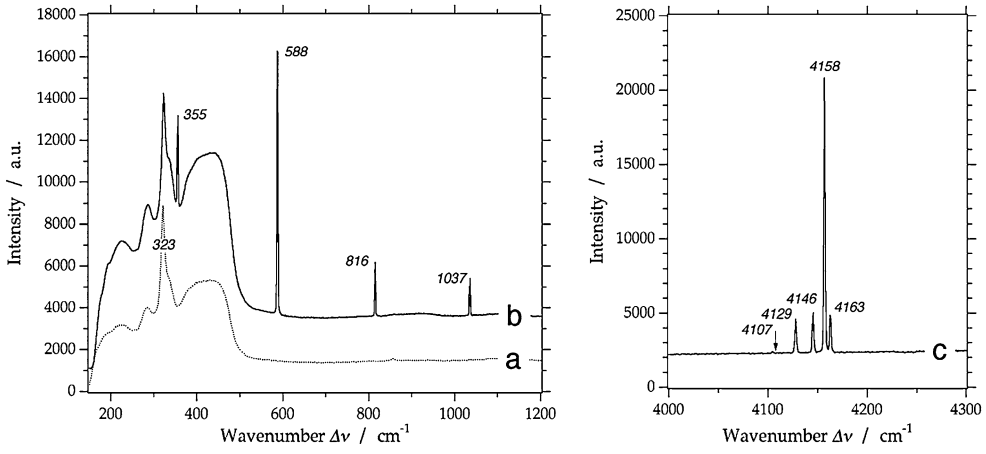

Fig. 29 Raman spectra ($\Delta\nu$) of fluorite (**a**) with a peak at 323 cm^{-1} and a weak fluorescence signal in the range of –500–500 cm^{-1} containing H_2-rich fluid inclusions (**b** and **c**). H_2 has five vibrational Raman bands (stretching) at relatively high wavenumbers (**c**)—4,107 (*1*), 4,129 (*12*), 4,146 (*15*), 4,158 (*100*) and 4,163 (*14*) cm^{-1}, in addition to four rotational Raman bands (*bending*) at lower wavenumbers (**b**)—355 (*23*), 588 (*68*), 816 (*14*) and 1,037 (*10*) cm^{-1}. *Italic numbers* in *brackets* are relative intensities

References

Anderko A, Pitzer KS (1993) Equation-of-state representation of phase equilibria and volumetric properties of the system NaCl–H_2O above 573 K. Geochim Cosmochim Acta 57:1657–1680

Anderson AT (2003) An introduction to melt (glass ± crystals) inclusions. In: Samson I, Anderson A, Marshall D (eds) Fluid inclusions, analysis and interpretation. Mineralogical Association of Canada, Ottawa, Short Course 32, pp. 353–364

Arzamaststev AA, Belyatsky BV, Arzamastseva LV (2000) Agpaitic magmatism in the northeastern Baltic Shield: a

study of the Niva intrusion, Kola Peninsula, Russia. Lithos 51:27–46
Ayllon F, Bakker RJ, Warr LN (2003) Re-equilibration of fluid inclusions in diagenetic-anchizonal rocks of the Ciñera-Matallana coal basin (NW Spain). Geofluids 3:49–68
Banks DA, Yardley BWD, Campbell AR, Jarvis KE (1994) REE composition of an aqueous magmatic fluid: a fluid inclusion study from the Capitan Pluton, New Mexico, U.S.A. Chem Geol 113:259–272
Baker T, van Achterberg E, Ryan CG, Lang JR (2004) Composition and evolution of ore fluids in a magmatic-hydrothermal skarn deposit. Geology 32:117–120
Bakker RJ (2003) Package FLUIDS 1. Computer programs for analysis of fluid inclusion data and for modelling bulk fluid properties. Chem Geol 194:3–23
Bakker RJ (2004) Raman spectra of fluid and crystal mixtures in the systems H_2O, H_2O–NaCl and H_2O–$MgCl_2$ at low temperatures: applications to fluid inclusion research. Can Mineral 42:1283–1314
Bakker RJ, Brown PE (2003) Computer modelling in fluid inclusion research. In: Samson I, Anderson A, Marshall D (eds) Fluid inclusions, analysis and interpretation. Mineralogical Association of Canada, Ottawa, Short Course 32, pp. 175–212
Bakker RJ, Diamond LW (2006) Estimation of volume fractions of liquid and vapor phases in fluid inclusions, and definition of inclusion shapes. Am Mineral 91:635–657
Bea F, Arzamastsev A, Montero P, Arzamastseva L (2001) Anomalous alkaline rocks of Soustov, Kola: evidence of mantle-derived metasomatic fluids affecting crustal materials. Contrib Mineral Petrol 140:554–566
Best MG (2003) Igneous and metamorphic petrology. Blackwell Publishing, Oxford, pp. 324–325
Bodnar RJ (1995) Fluid-inclusion evidence for a magmatic source for metals in porphyry copper deposits. In: Thompson JFH (ed) Magmas, fluids, and ore deposits. Mineralogical Association of Canada, Ottawa, Short Course 23, pp. 139–152
Bodnar RJ, Vityk MO (1994) Interpretation of microthermometric data for H_2O–NaCl fluid inclusions. In: de Vivo B, Frezzotti ML (eds) Fluid inclusions in minerals: methods and applications. IMA Short Course. Virginia Polytechnic Institute and State University press, Blacksburg, pp. 117–130
Campbell AR, Banks DA, Phillips RS, Yardley BWD (1995) Geochemistry of Th–U–REE mineralizing magmatic fluids, Captain Mountains, New Mexico. Econ Geol 90:1271–1287
Coats RP, Blissett AH (1971) Regional and economic geology of the Mount Painter Province. Geol Surv S Aust Bull 43:426
Cox RA, Dunning GR, Indares A (1998) Petrology and U–Pb geochronology of mafic, high-pressure, metamorphic coronites from the Tshenukutish domain, eastern Grenville Province. Precambrian Res 90:59–83
Della Ventura G, Bellatreccia F (1999) Zr- and LREE-rich titanite from TreCroci, Vico Volcanic complex (Latium, Italy). Mineral Mag 63:123–130
Dorais MJ (1993) Pyroxene in enclaves and syenites of the Red Hill Complex, New Hampshire: an ion and electron microprobe study. Contrib Mineral Petrol 114:130–138
Drake MJ, Weill DF (1972) New rare earth element standards for electron microprobe analysis. Chem Geol 10:179–181
Drexel JF, Major RB (1990) Mount Painter uranium—rare earth deposits. In: Hughes F (ed) Geology of the mineral deposits of Australia and Papua New guinea. Australian Institute of Mining and Metallurgy, Melbourne, pp. 993–998
Droop GTR (1987) A general equation for estimating Fe^{3+} concentrations in ferromagnesian silicates and oxides from microprobe analysis, using stoichiometric criteria. Mineral Mag 51:431–435
Dubessy J, Pagel M, Beny JM, Christensen H, Hickel B, Kosztolanyi C, Poty B (1988) Radiolysis evidenced by H_2–O_2 and H_2-bearing fluid inclusions in three uranium deposits. Geochim Cosmochim Acta 52:1155–1167
Elburg MA, Bons PD, Dougherty-Page J, Janka E, Neumann N, Schaefer B (2001) Age and metasomatic alteration of the Mt Neill Granite at Nooldoonooldoona Waterhole, Mt Painter Inlier, South Australia. Aust J Earth Sci 48:721–730
Elburg MA, Bons PD, Foden J, Brugger J (2003) A newly defined late Ordovician magmatic-thermal event in the Mt Painter Province, northern flinders Ranges, South Australia. Aust J Earth Sci 50:611–631
Falster AU, Simmons WB, Webber KL, Buchholz T (2000) Pegmatites and pegmatite minerals of the Wausau Complex, Marathon County, Wisconsin. Memorie della Società Italiana di Scienze Naturali e del Museo Civico di Storia Naturale di Milano 30:13–28
Ferreira VP, Sial AN, Whitney JA (1994) Large-scale silicate liquid immiscibility: a possible example from northeastern Brazil. Lithos 33:285–302
Florence FP, Darling RS, Orrell SE (1995) Moderate pressure metamorphism and anatexis due to anorthosite intrusion, western Adirondack Highlands. Contrib Mineral Petrol 121:424–436
Frezzotti ML (1992) Magmatic immiscibility and fluid phase evolution in the Mount Genis granite (souteastern Sardinia, Italia). Geochim Cosmochim Acta 56:21–33
Frezzotti ML (2001) Silicate-melt inclusions in magmatic rocks: application to petrology. Lithos 55:273–299
Gieré R, Williams CT (1992) REE-bearing minerals in a Ti-rich vein from the Adamello contact aureole (Italy). Contrib Mineral Petrol 112:83–100
Haar L, Gallagher JS, Kell GS (1984) NBS/NRC Steam Tables. Hemisphere Publ. Corp., Washington
Hunt JA, Kerrick DM (1977) The stability of sphene; experimental redetermination and geological implications. Geochim Cosmochim Acta 41:279–288
Idnurm M, Heinrich C (1993) A palaeomagnetic study of the hydrothermal activity and uranium mineralization of Mt Painter, South Australia. Aust J Earth Sci 40:87–101
Jahns RH (1955) The study of pegmatites. Econ Geol 50th Anniversary Volume, pp. 1025–1130
Khomyakov AP (1995) Mineralogy of hyperagpaitic alkaline rocks. Clarendon, London, p 223
Kogarko LN, Romanchev BP (1983) Phase equilibria in alkaline melts. Int Geol Rev 25:534–546
Konnerud-Madsen J, Rose-Hansen J (1982) Volatiles associated with alkaline igneous rift activity: fluid inclusions in the Ilímaussaq intrusion and the Gardar granitic complexes (South Greenland). Chem Geol 37:79–93
Kwak TAP, Abeysinghe PB (1987) Rare earth and uranium minerals present as daughter crystals in fluid inclusions, Mary Kathleen U–REE skarn, Queensland, Australia. Mineral Mag 363:665–670
Lister GF (1966) The composition and origin of selected iron–titanium deposits. Econ Geol 61:275–310
London D (2005) Granitic pegmatites: an assessment of current concepts and directions for the future. Lithos 80:281–303
Lottermoser BG (1987) A fluid inclusion study of the Tourmaline Hill Granite, Umberatana, South Australia: implications for hydrothermal activity and wallrock metasomatism. Mineral Petrol 36:135–148
Magde LS, Dick HJB, Hart SR (1995) Tectonics, alteration and the fractal distribution of hydrothermal veins in the lower ocean crust. Earth Planet Sci Lett 129:103–119

McLaren S, Dunlap WJ, Sandiford M, McDougall I (2002) Thermochronology of high heat-producing crust a Mount Painter, South Australia: implications for tectonic reactivation of continental interiors. Tectonics 21: article no. 1020

Moore JN, Adams MC, Anderson AJ (2000) The fluid inclusion and mineralogic record of the transformation from liquid- to vapor-dominated conditions in the Geysers Geothermal System, California. Econ Geol 95:1719–1737

Neumann N (2001) Geochemical and isotopic characteristics of South Australian Proterozoic granites: implications for the origin and evolution of high heat-producing terrains. PhD Thesis, University of Adelaide, Adelaide (unpublished)

Nijland TG, Touret JLR (2001) Replacement of graphic pegmatite by graphic albite–actinolite–clinopyroxene intergrowths (Mjåvatn, southern Norway). Eur J Mineral 13:41–50

Oliver NHS, Pearson PJ, Holcombe RJ, Ord A (1999) Mary Kathleen metamorphic-hydrothermal uranium-rare-earth element deposit: ore genesis and numerical model of coupled deformation and fluid flow. Aust J Earth Sci 46:467–484

Pan Y, Fleet ME, MacRae ND (1993) Late alteration in titanite (CaTiSiO5): redistribution and remobilization of rare earth elements and implications for U/Pb and Th/Pb geochronology and nuclear waste disposal. Geochim Cosmochim Acta 57:355–367

Panina LI (2005) Multiphase carbonate-salt immiscibility in carbonatite melts: data on melt inclusions from the Krestovskiy massif minerals (Polar Siberia). Contrib Mineral Petrol 150:19–36

Roedder E (1984) Fluid inclusions. Rev Mineral 12:644

Ruggieri G, Cathelineau M, Boiron M-C, Marignac C (1999) Boiling and fluid mixing in the chlorite zone of the Larderello geothermal system. Chem Geol 154:237–256

Scoon RN, Mitchell AA (1994) Discordant iron-rich ultramafic pegmatites in the Bushveld complex and their relationship to iron-rich intercumulus and residual liquids. J Petrol 35:881–917

Shmulovich KI, Tkachenko SI, Plyasunova NV (1995) Phase equilibria in fluid systems at high pressures and temperatures. In: Shmulovich KI, Yardley BWD, Gonchar GG (eds) Fluids in the crust, equilibrium and transport properties. Chapman and Hall, London, pp. 193–214

Simmons SF, Christenson BW (1994) Origins of calcite in a boiling geothermal system. Am J Sci 294:361–400

Smith MP, Henderson P, Campbell LS (2000) Fractionation of the REE during hydrothermal processes: constraints from the Bayan Obo Fe–REE–Nb deposit, Inner Mongolia, China. Geochim Cosmochim Acta 64:3141–3160

Sørensen H (1997) The agpaitic rocks—an overview. Mineral Mag 61:485–498

Spear FS (1981) An experimental study of hornblende stability and compositional variability in amphibolite. Am J Sci 281:697–734

Sterner SM, Bodnar RJ (1989) Synthetic fluid inclusions. VII Re-equilibration of fluid inclusions in quartz during laboratory-simulate metamorphic burial and uplift. J Metamorphic Geol 7:243–260

Sterner SM, Hall DL, Bodnar RJ (1988) Synthetic fluid inclusions: V: solubility relations in the system NaCl–KCl–H_2O under vapor-saturated conditions. Geochim Cosmochim Acta 52:989–1005

Teale GS (1993) The Nooldoonooldoona Trondhjemite and other newly recognised Mesoproterozoic intrusives in the Mount Painter Province. Geol Surv S Aust Q Geol Notes 125:20–31

Teale GS, Lottermoser BG (1987) Palaeozoic granites of the Umberatana region, South Australia; the role of volatiles in the crystallization of some alkaline–peralkaline granites. Geolog Rundsch 76:857–868

Thompson JFH (ed) (1995) Magmas, fluids, and ore deposits. Mineralogical Association of Canada, Ottawa, Short Course 23, 525 pp

Tsujimori T (1997) Omphacite–diopside vein in an omphacitite block from the Osayama serpentinite melange, Sangun-Renge metamorphic belt, southwestern Japan. Mineral Mag 61:845–852

Viljoen MJ, Scoon RN (1985) The distribution and main geologic features of discordant bodies of iron-rich ultramafic pegmatite in the Bushveld Complex. Econ Geol 80:1109–1128

Wallace GM, Whalen JB, Martin RF (1990) Agpaitic and miaskitic nepheline syenites of the McGerrigle plutonic complex, Gaspé, Quebec: an unusal petrological association. Can Mineral 28:251–266

Wang S, Williams PJ (2001) Geochemistry and origin of Proterozoic skarns at the Mount Elliott Cu–Au(–Co–Ni) deposit, Cloncurry district, NW Queensland, Australia. Mineralium Deposita 36:109–124

Weisbrod A (1981) Fluid inclusions in shallow intrusives. In: Hollister LS, Crawford ML (eds) Fluid inclusions: application to petrology. Mineralogical Association of Canada, Ottawa, Short Course 7, pp. 241–271

Winkler HF (1979) Petrogenesis of metamorphic rocks. Springer, Berlin Heidelberg New York, p 348

Xirouchakis D, Lindsley DH, Andersen DJ (2001a) Assemblages with titanite ($CaTiOSiO_4$), Ca–Mg–Fe olivine and pyroxenes, Fe–Mg–Ti oxides, and quartz: Part I. Theory. Am Mineral 86:247–253

Xirouchakis D, Lindsley DH, Frost BR (2001b) Assemblages with titanite ($CaTiOSiO_4$), Ca–Mg–Fe olivine and pyroxene, Fe–Mg–Ti oxides, and quartz: Part II. Application. Am Mineral 86:254–264

Zabavnikova NI (1957) Diadochic substitutions in sphene. Geochem 3:271–278